Differentiation Conditions of a Basaltic Magma from Santorini, and its Bearing on the Production of Andesite in Arc Settings

Joan Andújar[1,2,3]*, Bruno Scaillet[1,2,3], Michel Pichavant[1,2,3] and Timothy H. Druitt[4]

[1]Université d'Orléans, ISTO, UMR 7327, 45071 Orléans, France, [2]CNRS/INSU, ISTO, UMR 7327, 45071 Orléans, France, [3]BRGM, ISTO, UMR 7327, BP 36009, 45060 Orléans, France and [4]Laboratoire Magmas et Volcans, Université Blaise Pascal–CNRS–IRD, OPGC, 5 Rue Kessler, 63038 Clermond-Ferrand, France

*Corresponding author. Telephone: (+33) 2 38 25 53 87. Fax: (+33) 02 38 63 64 88.
E-mail: Juan.Andujar@cnrs-orleans.fr

ABSTRACT

Santorini volcano in the Aegean region (Greece) is characterized by andesitic- to silicic-dominated explosive activity and caldera-forming eruptions, sourced from magmatic reservoirs located at various structural levels beneath the volcano. There is a good understanding of the silica-rich magmatism of the island whereas the andesite-dominated volcanism and the petrogenesis of the parental mafic magmas are still poorly understood. To fill this gap we have performed crystallization experiments on a representative basalt from Santorini with the aim of determining the conditions of differentiation (pressure, temperature, volatile fugacities) and the parental magma relationship with the andesitic eruptive rocks. Experiments were carried out between 975 and 1040°C, in the pressure range 100–400 MPa, fO_2 from QFM to $NNO + 3.5$ (where QFM is quartz–fayalite–magnetite and NNO is nickel–nickel oxide), with H_2O_{melt} contents varying from saturation to nominally dry conditions. The results show that basalt phenocrysts within the basalt crystallized at around 1040°C in a magma storage reservoir located at a depth equivalent to 200–400 MPa pressure, with 3–5 wt % dissolved H_2O, and fO_2 around QFM. Comparison with the xenocryst and phenocryst assemblages of the Upper Scoria 1 andesite shows that andesitic liquids are produced by fractionation of a similar basalt at 1000°C and 400 MPa, following 60–80 wt % crystallization of an ol + cpx + plag + Ti-mag + opx ± pig–ilm assemblage, with melt water contents around 4–6 wt %. At Santorini, the andesitic low-viscosity and water-rich residual liquids produced at these depths segregate from the parent basaltic mush and feed the shallow magma reservoirs, eventually erupting upon mixing with resident magma. Changes in prevailing oxygen fugacity may control the tholeiitic–calc-alkaline character of Santorini magmas, explaining the compositional and mineralogical differences observed between the recent Thyra and old eruptive products from Akrotiri.

Key words: phase equilibria; basalt; andesite; liquid line of descent; experimental petrology; Santorini

INTRODUCTION

Caldera-forming eruptions are among the most hazardous phenomena on Earth. They are characterized by the emission of huge amounts of magma and gas (e.g. Mt Mazama: Bacon & Druitt, 1988; Druitt & Bacon, 1989; Tambora: Self *et al.*, 2004; Krakatoa: Mandeville *et al.*,

1996; Fish Canyon Tuff: Bachmann *et al.*, 2002; Bishop Tuff: Hildreth & Wilson, 2007) and can affect the climate at a global scale and be harmful to human life and related infrastructure. This is the case of Santorini volcano, in the Aegean region of Greece, the explosive activity of which has led to several caldera-forming

events. The last and largest of these eruptions occurred at around 3·6 ka (the so-called Minoan eruption; Heiken & McCoy, 1984; Druitt, 2014), with 30–60 km³ of ejected rhyodacitic magma. Although several studies have focused on the petrogenesis of the silicic magmas (Cottrell *et al.*, 1999; Druitt *et al.*, 1999; Gertisser *et al.*, 2009; Cadoux *et al.*, 2014), less attention has been paid to the more mafic compositions, even though the volcanic activity at Santorini has involved several large andesite-dominated explosive eruptions (i.e. the Upper Scoria eruptions; Druitt *et al.*, 1999) and effusive activity involving magmas ranging from basalt to dacite in composition. The conditions of evolution from basalt to more evolved compositions are therefore still unclear. To improve our knowledge of andesitic volcanism at Santorini, and at volcanic arcs in general, we have investigated experimentally the phase relationships of a representative basalt from Santorini, with the aim of determining the conditions of differentiation (pressure, temperature, volatile fugacities) that generate the andesitic magmas erupted there. To achieve this objective, we have identified the conditions under which basaltic-andesite to andesite liquids are generated by fractional crystallization of the basalt, and have refined this estimate by comparing the phenocryst and xenocryst populations of a typical Santorini andesite (Upper Scoria 1 eruption) with the experimental phases of basaltic charges with residual andesitic liquids. Our results show that mantle-derived basalts stagnate at depths of 12–14 km (400 MPa), where they fractionate to yield basaltic andesite liquids (55–58 wt % SiO₂) with ∼4–6 wt % H₂O$_{melt}$ at around 1000°C and at an *f*O₂ near QFM (quartz–fayalite–magnetite; ±0·3 log units). This is achieved by crystallizing about 60 wt % of olivine (ol), clinopyroxene (cpx), plagioclase (plag), orthopyroxene (opx), Ti-rich magnetite ± pigeonite (pig), and ilmenite (ilm).

GEOLOGICAL SETTING

The geology and tectonic setting of Santorini have been the focus of many studies, which are briefly summarized below. The Santorini islands belong to the Cyclades archipelago. They constitute the most active volcanic complex of the South Aegean volcanic arc, which is related to the NE-directed subduction of the African plate beneath the southern margin of the Eurasian plate (Le Pichon & Angelier, 1979; Jolivet & Faccenna, 2000; Papazachos *et al.*, 2000; Reilinger *et al.*, 2010). The volcanic island is built on a 23 km thick continental crust made of an upper layer of Mesozoic to Cenozoic marbles and phyllites, and a lower layer of Precambrian to Paleozoic garnet-bearing gneisses and mica schists (Nicholls, 1971*b*; Druitt *et al.*, 1999). The volcanic history of Santorini can be summarized as follows (Druitt *et al.*, 1999): activity began at about 650 ka with the eruption of hornblende-bearing rhyolites, rhyodacites and minor andesites of calc-alkaline affinity. From 550 ka onwards, the volcano erupted magmas

ranging from basalt to rhyodacite in composition, hornblende became scarce as a phenocryst phase, and the magmas became tholeiitic to transitional tholeiitic–calc-alkaline in character. Around 360 ka, the activity became highly explosive, with the alternation of plinian eruptions with interplinian periods of constructional activity involving effusive and weakly explosive emissions. Direct field evidence exists for at least four caldera collapse events associated with large plinian eruptions. Following the Minoan eruption at about 3·6 ka, subaerial volcanic activity resumed within the caldera at 197 BC and continued until recent times (Pyle & Elliott, 2006). The products of this historical volcanism have built up an ∼3 km³ intracaldera edifice, the summit of which forms the islands of Palea Kameni and Nea Kameni. The last eruption of the Kameni Volcano took place in 1950. A period of caldera unrest, involving uplift and increased seismicity, took place at Santorini in 2011–2012 (Parks *et al.*, 2012).

The products of the <360 ka large explosive eruptions range from andesitic to rhyodacitic in composition (Huijsmans *et al.*, 1988; Huijsmans & Barton, 1989; Druitt *et al.*, 1999). Large explosive eruptions of andesitic magma include the Upper Scoria 1 (80 ka; Keller *et al.*, 2000; Vespa *et al.*, 2006) and Upper Scoria 2 (54 ± 3 ka; Druitt *et al.*, 1999) eruptions. Large silicic eruptions include the Lower Pumice 1 (184 ka; Keller *et al.*, 2000; Gertisser *et al.*, 2009), Lower Pumice 2 (172 ka; Keller *et al.*, 2000; Gertisser *et al.*, 2009), Cape Riva (21·8 ± 0·4 ka; Fabbro *et al.*, 2013) and Minoan (3·6 ka) eruptions. The large silicic reservoirs were dominated by rhyodacitic magma, which, immediately prior to eruption, was intruded by basaltic to andesitic magmas, which are found as mafic blebs or bands dispersed within the main silicic volume (Nicholls, 1971*a*; Huijsmans *et al.*, 1988; Cottrell *et al.*, 1999; Druitt *et al.*, 1999; Gertisser *et al.*, 2009).

Previous constraints on storage conditions
Constraints on pre-eruptive conditions for Santorini magmas have been obtained previously by applying geothermometers and mineral–liquid equilibria, except for the silicic components, for which experimental phase equilibria were investigated by Cottrell *et al.* (1999) and Cadoux *et al.* (2014). Coexisting Fe–Ti oxides in dacitic to rhyodacitic products yield temperatures of 825–985°C (Gardner *et al.*, 1996; Cottrell *et al.*, 1999; Druitt *et al.*, 1999; Gertisser *et al.*, 2009; Cadoux *et al.*, 2014). Estimates for the more mafic compositions (50–60 wt % SiO₂) based on olivine–melt and clinopyroxene–orthopyroxene geothermometers yield temperatures between 980 and 1030°C for andesites (i.e. 1000°C for Upper Scoria 1; Gardner *et al.*. 1996) and up to 1200°C for basaltic compositions (Huijsmans, 1985; Gertisser *et al.*, 2009). Such estimates are in general agreement with those obtained by Michaud *et al.* (2000), based on melt inclusion homogenization during heating stage experiments, which yield temperatures of 850–900°C for rhyodacites, 985–1005°C for andesites,

and 1085–1105°C for basalts. Magmatic water contents (H_2O_{melt}) were obtained by Fourier transform infrared (FTIR) analysis of melt inclusions and by experimental phase equilibria determinations for several rhyodacitic eruptions (Cottrell *et al.*, 1999; Cadoux *et al.*, 2014). Melt inclusions within phenocrysts in the Upper Scoria 1 andesite and within crystals in mafic blebs from the Lower Pumice 2 eruption yield H_2O_{melt} of about 3–3·8 wt %, respectively (Gardner *et al.*, 1996; Gertisser *et al.*, 2009; Cadoux *et al.*, 2014), whereas H_2O_{melt} of rhyodacitic magmas ranges from 3 to 6·5 wt % (Minoan, Cape Riva, Lower Pumice 2, lower Pumice 1; Cottrell *et al.*, 1999; Gertisser *et al.*, 2009; Cadoux *et al.*, 2014). Pressure estimates using Al-in-hornblende and phase equilibrium experiments on rhyodacitic eruptive products range between 50 and 400 MPa (Cottrell *et al.*, 1999; Gertisser *et al.*, 2009; Cadoux *et al.*, 2014). Based on the high water contents of the melt inclusions and the presence of xenocrystic amphibole in Minoan rhyodacitic products, Cottrell *et al.* (1999) inferred an initial storage pressure of 200 MPa for this eruption. Phase equilibrium experiments performed by those researchers led them to conclude that the Minoan magma rose to shallower depths (50 MPa) a few months prior to the eruption. However, recent detailed investigations by Cadoux *et al.* (2014), which combined petrological studies and phase equilibrium experiments on products from Minoan and other major rhyodacitic eruptions at Santorini (Cape Riva, Lower Pumice 2, Lower Pumice 1), concluded that all these magmas were stored at the same pressure (∼200 MPa), and that the change in storage conditions previously inferred by Cottrell *et al.* (1999) for the Minoan magma is not required to explain the petrological attributes of this eruption. Lastly, fO_2 estimates based on coexisting Fe–Ti oxides range between QFM – 0·5 and NNO + 0·5 (where NNO is nickel–nickel oxide) for mafic to silicic compositions (Cottrell *et al.*, 1999; Gertisser *et al.*, 2009; Cadoux *et al.*, 2014; Druitt, 2014).

Petrological observations of selected samples

To constrain the conditions of storage and evolution of basaltic magmas at Santorini we have performed phase equilibrium experiments on a basaltic sample from the 344 ± 24 ka Balos Bay cinder cone (Fig. 1; Nicholls, 1971a; Druitt *et al.*, 1999). The run products were compared with phenocryst, xenocryst and melt compositions of the Upper Scoria 1 andesite, to investigate the genetic relationships between basaltic and andesitic compositions (Fig. 1; Druitt *et al.*, 1999). Bulk-rock compositions of both rocks (Balos Bay basalt and Upper Scoria 1 andesite) obtained by inductively coupled plasma mass spectrometry (ICP-MS) analysis are given in Tables 1 and 2, and are in agreement with those for the same rocks in previous studies (Nicholls, 1971a; Druitt *et al.*, 1999). The mineralogy of each sample was examined in detail using both petrographic and scanning electron microscopes (SEM) for several thin sections from each rock. This allowed us to identify the

phenocryst and xenocryst assemblages in each sample, and to document the compositional zonation of minerals. The crystal contents of the Balos basalt and Upper Scoria 1 samples were determined by SEM image analysis, and converted to weight per cent using the mineral densities of Deer *et al.* (1972) (Table 1). Phenocrysts and xenocrysts in the basalt and andesite together provide information on the conditions of magma generation and storage at Santorini. The compositions of the main mineral phases determined by electron microprobe analysis (EMPA) are summarized in Tables 1 and 2 and plotted in Figs 2–7.

Basaltic sample: Balos cinder cone

The rock contains about 41 wt % crystals, of which 7 wt % are macrophenocrysts (0·5–1 mm) of olivine (Fo_{74-78}) showing little compositional variation (Fo_{74-76}) between and within crystals (Fig. 2b). There are 32 wt % (0·5–0·3 mm) microphenocrysts of plagioclase (∼300–500 µm) with An_{78-80} cores and An_{72} rims (Fig. 2e), along with 2 wt % clinopyroxene [$En_{43 \pm 2·6}Fs_{11 \pm 1·2}Wo_{45 \pm 3·5}$, Mg# 80 ± 1·6; Mg# = 100 Mg/(Mg + Fe$_{tot}$)]. Magnetite (Mg# 1·9) and ilmenite (Mg# 1·4; 50·5 TiO$_2$ wt %) occur in trace amounts. The groundmass consists predominantly of microlites (≤0·05 mm) of plagioclase, orthopyroxene/pigeonite ($En_{69}Fs_{22}Wo_{7·8}$, Mg# 76; Fig. 2), clinopyroxene and magnetite. In addition to this equilibrium-looking assemblage, partly resorbed olivine crystals showing slight inverse zoning from Fo_{76} to Fo_{78} (Fig. 2b) occur along with a few resorbed and reversely zoned clinopyroxenes (core: $En_{42}Fs_{10}Wo_{47}$, Mg# 80; rim: $En_{44}Fs_8Wo_{48}$, Mg# 84) (Fig. 2d), and rare calcic plagioclase crystals with An_{85-90} cores and narrow An_{79} rims (Fig. 2e).

These observations are interpreted to indicate that the Balos basalt phenocryst assemblage was dominated by olivine, clinopyroxene, plagioclase and magnetite, whereas minor ilmenite and orthopyroxene/pigeonite crystallized as groundmass phases at temperatures lower than that of the phenocrysts. The presence of a few inversely zoned olivine and clinopyroxene phenocrysts possibly records a previous episode of mixing with a more mafic magma from which the high-An plagioclase cores were derived. The An-poor narrow rims of the Ca-rich plagioclase match the main basalt plagioclase composition, and suggest partial equilibration prior to the eruption (Fig. 2; see below).

Andesitic sample: Upper Scoria 1 (USC-1)

The USC-1 andesite (Table 2) contains 28 wt % phenocrysts of euhedral to subhedral plagioclase (16 wt %, An_{53}), augite (8 wt %, $En_{42}Fs_{21}Wo_{37}$, Mg# 67), magnetite (3 wt %) and lesser amounts of orthopyroxene (1·4 wt %, $En_{65}Fs_{29}Wo_4$) set in a microcrystalline groundmass of plagioclase, clinopyroxene, magnetite and highly vesiculated glass (Fig. 3a).

USC-1 pyroxenes

Pyroxenes display a wide range of compositions, including augite, diopside, pigeonite and orthopyroxene, as

well as complex textural features (Table 2; Fig. 4). The modal distribution of Mg# in clinopyroxene shows a main population at Mg# 61–71 (Fig. 4a), with a discontinuous tail towards more magnesian values. On a modal plot for opx–pigeonite, three distinct peaks are observed at Mg# 58, 70 and 75–81 (Fig. 4b and c).

In detail, augite occurs as euhedral to subhedral crystals between 50 and 150 μm in size; the dominant population has an average composition of $En_{42}Fs_{21}Wo_{37}$, Mg# 67 $\pm$ 1 (Table 2, Figs 3 and 4a–c), and appears either as isolated, normally zoned, crystals (cores of $En_{44}Fs_{19}Wo_{37}$, Mg# 70 to rims of $En_{42}Fs_{21}Wo_{37}$, Mg# 67 $\pm$ 1) or mantling Mg-poorer augite ($En_{38}Fs_{23}Wo_{39}$, Mg# 63) or pigeonite cores ($En_{55}Fs_{28}Wo_{16}$, Mg# 67) (Figs 4 and 5; Table 2). Apart from these cores, pigeonite also appears as isolated and partially resorbed crystals with compositions ranging from $En_{55}Fs_{28}Wo_{16}$, Mg# 66, to $En_{60}Fs_{30}Wo_{8}$, Mg# 67 (Table 2; Fig. 5).

Orthopyroxene is $\sim$200 μm in size and is present as resorbed crystals of composition $En_{55}Fs_{40}Wo_{4}$, Mg# 58,

mantled by $En_{65}Fs_{29}Wo_{4}$, Mg #68 (Fig. 6), which in some cases is overgrown by augite ($En_{42-44}Fs_{21-19}Wo_{37}$, Mg# 67–70; Fig. 6c). Such textural relationships, and the lack of reaction rims between the Mg-rich orthopyroxene ($En_{65}Fs_{29}Wo_{4}$, Mg# 68) and the augite ($En_{42-44}Fs_{21-19}Wo_{37}$, Mg# 67–70), suggest that these two phases either co-crystallized (sometimes on the $En_{55}Fs_{40}Wo_{4}$, Mg# 58 resorbed opx; Fig. 6c) or appeared in close succession to each other.

Finally, diopsides of composition $En_{43-45}Fs_{10-14}Wo_{43-45}$, Mg# 75–81, are present as large (0·5–1 mm) euhedral to partially rounded crystals, showing small compositional variations. Some single crystals have narrow rims that reach the main augite composition ($En_{42}Fs_{21}Wo_{37}$, Mg# 67 $\pm$ 1; Figs 3e, f and 4d).

USC-1 plagioclase, magnetite and olivine

Plagioclase occurs as two distinct populations: euhedral crystals (100–300 μm) of near-uniform composition ($An_{53 \pm 2·5}$; Table 2; Fig. 7a), and zoned crystals
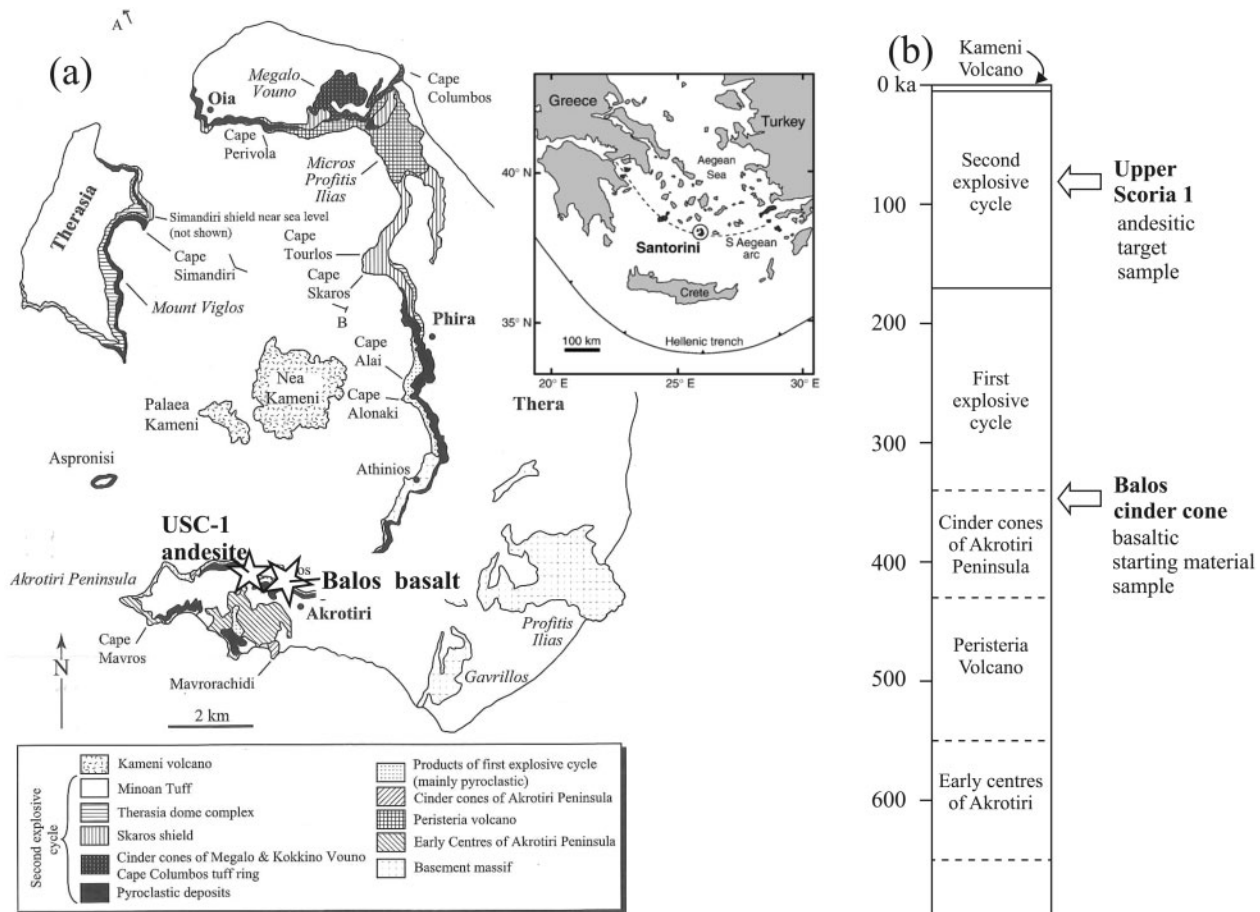

Fig. 1. (a) Simplified geological map of Santorini after Druitt _et al._ (1999) showing sample locations. Inset map shows the location of Santorini, modified from Gertisser _et al._ (2009). (b) Schematic stratigraphy of Santorini volcanic products, summarized from Druitt _et al._ (1999). The Balos cinder cone (344 $\pm$ 24 ka) and Upper Scoria 1 eruption (80 ka) were the sources for the basaltic and andesitic samples used in this study, respectively. (c) TiO_2 (wt %) and (d) FeO_{tot} (wt %) vs SiO_2 (wt %) for Santorini eruptive rocks. The fractionation trend for the Santorini magmas is shown as a grey arrow, whereas mixing models for Cape Riva and Upper Therasia andesites (grey dashed field) are shown as black lines. It should be noted that the Balos basalt and Upper Scoria 1 (USC-1) bulk-rock compositions plot on the fractionation trend, indicating that both samples are true liquids and genetically linked (see text for details).
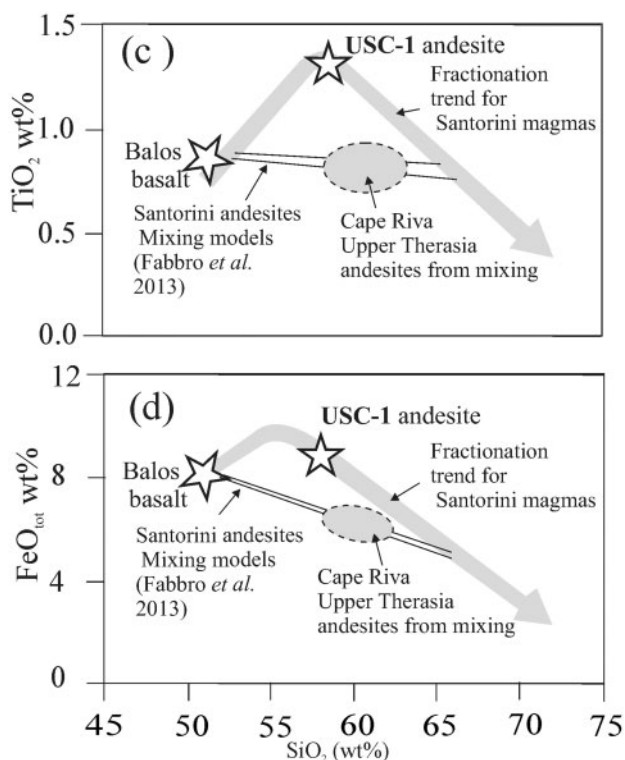
(continued)

Fig. 1. Continued

($\geq$500 μm) with cores of $An_{91 \pm 3}$ and narrow rims of variable composition (An_{53-75}; Figs 3b and 7b). Magnetite is homogeneous in composition, with Mg# of 6·17 and a TiO_2 content of 15 wt % (Table 2). Olivine appears as partially resorbed crystals with sizes of 50–150 μm and compositions of Fo_{63-68} (Table 2, Fig. 3c and d).

Origin of crystals in the andesite
Based on the above textural relationships, modal abundances and dominant mineral compositions observed in USC-1 sample (Figs 2–7) we infer that the Ca-poor plagioclase (An_{53}), Mg-poor augite ($En_{42}Fs_{21}Wo_{37}$, Mg# 67), magnetite and $En_{65}Fs_{29}Wo_4$, Mg#68 orthopyroxene probably crystallized from the host andesitic magma. In contrast, a xenocrystic origin for olivine, pigeonite (found as pyroxene cores and as isolated crystals; Fig. 5), diopside and An-rich plagioclase ($An_{91 \pm 3}$) is inferred based on the following lines of evidence: (1) as shown below, both pigeonite and olivine readily crystallize in the experiments performed on the Balos basalt; (2) the compositions (and zonation) of the diopside and $An_{91 \pm 3}$ plagioclase found in the andesite are identical to those in the Balos basalt (compare Figs 2d, 4d and 7b), indicating that these mineral compositions were probably derived from a basaltic magma with a composition similar to that of the Balos basalt (note that the cpx compositions plot in the field defined by Balos diopside phenocrysts in Fig. 4c); (3) the frequent presence, on these diopside and plagioclase xenocrysts, of

narrow rims matching the composition of the main augite–plagioclase population suggests re-equilibration with the host andesitic melt; however, the lack of such rims or resorbed textures on some olivine and pigeonite crystals (Figs 3–7) shows that not all xenocrysts had time to react; (4) the resorbed texture of the $En_{55}Fs_{40}Wo_4$, Mg# 58 orthopyroxenes in USC-1 and the fact that they are commonly mantled by a more Mg-rich composition also suggest a xenocrystic origin for such orthopyroxenes, which are similar to those of Santorini dacites (e.g. the Middle Pumice unit; Druitt *et al.*, 1999).

On this basis, we have calculated by mass balance the amount of xenocrysts in the USC-1 sample to estimate their effect on the whole-rock composition. The results indicate that, despite the large sizes of these crystals (>1 mm; e.g. diopside in Fig. 3), they represent less than 1·5 vol. % of the whole sample and so have little compositional effect on the bulk-rock composition. Along with the relatively small amount of phenocrysts, this indicates that the USC-1 bulk-rock composition is close to that of a liquid. This is an important inference for our subsequent (see below) comparison of USC-1 bulk-rock and phenocryst chemistry with the products of the Balos basalt crystallization experiments (see also Pichavant *et al.*, 2007).

Phenocryst proportions and compositions (excluding xenocrysts) were used to calculate, by mass balance, the residual melt chemistry, which is andesitic in composition and more evolved than the bulk-rock itself: 63 wt % SiO_2, 7 wt % FeO_{tot}, 1·8 wt % MgO and 6·6 wt % $(Na_2O + K_2O)$ (Table 2).

Liquid line of descent (LLD) at Santorini: the Balos basalt and significance of the USC-1 andesite

Although magma mixing is often proposed as one of the main mechanisms of andesite production in arc settings (e.g. Eichelberger, 1978; Reubi & Blundy, 2009; Laumonier *et al.*, 2014), petrological and geochemical data have shown that the basalt to rhyodacite series at Santorini is generated mainly by fractional crystallization, as described by, for example, Nicholls (1971*a*), Barton *et al.* (1983), Mann (1983), Huijsmans & Barton (1989), Huijsmans *et al.* (1989), Michaud *et al.* (2000) and Zellmer *et al.* (2000). According to those researchers the evolution from basalt to andesite is driven by the fractionation of olivine, calcic plagioclase and clinopyroxene, followed by plagioclase, orthopyroxene, $\pm$titanomagnetite and apatite. This defines a liquid line of descent that is initially characterized by an enrichment in Fe, Ti and P, as these elements behave incompatibly during the early stages of magma evolution (grey arrows in Fig. 1c and d) until andesitic compositions (SiO_2 > 58 wt %) are reached. Beyond this the residual melts are depleted in FeO_{tot} and TiO_2 owing to the crystallization of Ti-magnetite and ilmenite, together with orthopyroxene, clinopyroxene, plagioclase and apatite (Fig. 1c and d; Nicholls, 1971*a*; Barton *et al.*, 1983; Mann, 1983; Huijsmans & Barton, 1989;

Table 1: Major element composition of the natural Balos basalt sample: bulk-rock, starting material and mineral phases

	Bulk-rock	Starting material	SD	magnetite	SD	ilmenite	SD	olivine	SD	diopside	SD	opx	SD	plag	SD	plag xeno	SD
n:		10		7		5		32		29		2		37		9	
SiO_2	51·1	51·8	0·2	0·11	0·06	0·03	0·03	37·69	0·45	48·81	1·51	53·29	0·19	47·70	0·47	45·05	0·45
TiO_2	0·91	0·96	0·04	7·88	0·84	50·47	1·88	0·02	0·03	0·89	0·17	0·44	0·08	0·03	0·02	0·02	0·02
Al_2O_3	18·2	17·7	0·2	2·67	1·11	0·09	0·04	0·01	0·02	5·03	1·54	0·72	0·01	31·75	0·26	33·62	0·22
MgO	6·77	6·53	0·09	0·96	0·71	1·18	0·32	35·73	0·71	14·45	0·93	23·58	0·22	0·05	0·02	0·03	0·02
CaO	11·2	11·2	0·2	0·16	0·16	0·04	0·04	0·19	0·09	20·95	1·79	3·72	0·10	15·95	0·27	17·98	0·23
MnO	0·16	0·09	0·05	0·21	0·15	0·49	0·11	0·48	0·07	0·21	0·15	0·49	0·14	0·02	0·02	0·03	0·04
FeO_{tot}	8·21	8·28	0·22	87·99	2·32	47·69	2·23	21·09	0·65	6·48	0·75	13·66	0·31	0·61	0·08	0·45	0·08
Na_2O	2·83	2·74	0·06	0·00	0·00	0·01	0·01	0·01	0·01	0·32	0·06	0·04	0·01	2·29	0·13	1·20	0·07
K_2O	0·5	0·57	0·05	0·02	0·02	0·03	0·03	0·01	0·02	0·05	0·23	0·00	0·00	0·12	0·03	0·03	0·01
P_2O_5	0·13	0·20	0·08	—	—	—	—	—	—	—	—	—	—	—	—	—	—
Sum	100·04	100		100·0	0·0	100·0	0·0	95·3	0·8	97·2	1·7	95·9	1·0	98·5	0·5	98·40	0·56
Mg#				1·9	0·5	1·4	0·5	—	—	79·9	1·6	75·5	0·2				
Mol %																	
Fo								74·9	1·1								
En										43·4	2·6	69·0	0·5				
Fs										10·9	1·2	22·4	0·1				
Wo										45·3	3·5	7·8	0·1				
An														78·8	1·2	89·07	0·66
Ab														21·5	1·7	10·78	0·65
Or														0·8	0·2	0·15	0·06
Phase proportions (wt %)				trace		trace		6·6		1·9		trace		31·5			

Bulk-rock analysed by inductively coupled plasma mass spectrometry. *n*, number of analyses. SD, standard deviation. FeO_{tot}, total iron reported as FeO. Fo (mol %) $= 100\,Mg/(Mg + Fe_{tot})$ in olivine. En, Fs and Wo were calculated as in the study by Morimoto (1989). Mg# $= 100[Mg/(Mg + Fe_{tot})]$. An $= 100[Ca/(Ca + Na + K)]$; Ab $= 100[Na/(Ca + Na + K)]$; Or $= 100[K/(Ca + Na + K)]$. End-members calculated as in the study by Deer *et al.* (1972). trace, crystal abundance <0.5 wt %. opx, orthopyroxene; plag, plagioclase; xeno, xenocryst.

Huijsmans *et al.*, 1989; Michaud *et al.*, 2000; Zellmer *et al.*, 2000). Notwithstanding, though less abundant than those originating by fractionation, some andesites from Santorini exhibit clear textural and geochemical evidence of being the products of mixing between basaltic and silicic magmas (e.g. Cape Riva and Upper Therasia andesites; Druitt *et al.*, 1999; Fabbro *et al.*, 2013). Such mixed andesites clearly plot below the liquid line of descent (LLD) defined by most Santorini magmas (grey arrows in Fig. 1c and d), being characterized by lower Ti, P and Fe contents and bimodal (disequilibrium) mineral assemblages (Nicholls, 1971*a*; Druitt *et al.*, 1999; Fabbro *et al.*, 2013). To ascertain the representativity (Balos basalt) or significance (USC-1 andesite) of the rocks employed in our study, their compositions are plotted on SiO_2 vs FeO_{tot} and TiO_2 diagrams along with the LLD of the Santorini magmas (Fig. 1c and d). The Balos basalt plots at the beginning of the Santorini fractionation trend, whereas USC-1 plots at the TiO_2 and FeO_{tot} enrichment peak, far away from the field defined by the hybrid andesites. This shows that (1) the Balos sample has a bulk-rock composition representative of basaltic magmas at Santorini, and is thus a good parent magma candidate for the Santorini magma series, and (2) despite the presence of xenocrystic minerals the USC-1 composition is similar to fractionated andesitic melts typically found at this volcanic system.

We conclude that both samples can be genetically linked by a simple fractional crystallization processes, and this is the working hypothesis of our experimental approach.

EXPERIMENTAL AND ANALYTICAL TECHNIQUES

The dry starting glass for our experimental study was obtained by crushing and milling several pieces of the Balos basalt (about 10 g), followed by a two-step fusion of the resulting powder (with grinding between the two fusion stages) in a platinum crucible at 1400°C and atmospheric pressure for 3 h. Electron microprobe analysis of the dry glass showed it to be homogeneous and similar to the X-ray fluorescence (XRF) bulk-rock analysis of the sample (Table 1). The basaltic glass was then ground and stored at 120°C in an oven to avoid atmospheric hydration.

Capsule preparation

The powder was loaded into 1·5 cm long, 2·5 mm inner diameter, 0·2 mm walled, Au capsules to minimize Fe loss under reduced conditions. All capsules were prepared following the procedure described by Scaillet *et al.* (1995) and Andújar & Scaillet (2012), where H_2O is added first, followed by silver oxalate as a source for CO_2 in H_2O-undersaturated runs. The amount of $H_2O + CO_2$ added to the capsule and the fluid/silicate ratio were maintained constant by adding 3 ± 0.5 mg of fluid ($H_2O + CO_2$) and 30 mg of glass powder, which ensured that fluid-saturated conditions were always achieved (e.g. Scaillet *et al.*, 1995; Andújar & Scaillet, 2012; Cadoux *et al.*, 2014).

The capsules were then arc-welded and left in an oven at 100°C for a few hours to homogenize the H_2O distribution within the charges before the experiments. For all charges reported in Table 3, the weight of the capsules prior to and after the experiments agreed to

Table 2: Major element composition of the natural Upper Scoria 1 andesite sample: bulk-rock, starting material and mineral phases

	Bulk-rock	glass*	magnetite	SD	plag	SD	augite Mg# 67	SD	augite Mg# 70	SD	augite Mg# 63	SD	opx	SD
n:			6		85		67		17		11		5	
SiO_2	58·52	62·79	0·11	0·02	55·05	1·44	49·25	0·73	48·97	1·14	48·38	1·41	52·05	0·72
TiO_2	1·30	0·98	15·14	2·29	0·07	0·13	1·01	0·12	0·97	0·13	1·10	0·46	0·33	0·06
Al_2O_3	16·04	15·82	3·02	0·56	26·61	0·74	3·54	0·66	3·02	0·64	3·36	1·41	1·09	0·51
MgO	2·84	1·78	2·64	0·50	0·08	0·11	14·20	0·44	14·65	0·32	12·70	0·72	23·49	0·77
CaO	6·55	4·82	0·07	0·06	10·40	0·54	17·46	0·81	17·36	0·72	18·28	1·03	2·09	0·19
MnO	0·19	0·19	0·50	0·22	0·04	0·05	0·42	0·12	0·37	0·08	0·51	0·16	0·63	0·10
FeO_{tot}	8·74	7·01	71·45	1·34	0·62	0·57	12·40	0·50	11·09	0·28	13·55	0·86	18·85	0·69
Na_2O	4·19	4·70	0·03	0·04	5·03	0·31	0·31	0·05	0·23	0·03	0·31	0·10	0·07	0·10
K_2O	1·40	1·90	0·02	0·03	0·20	0·11	0·02	0·02	0·02	0·02	0·06	0·13	0·02	0·03
P_2O_5	0·23													
Sum	100	100	93·09	1·60	98·27	1·37	92·68	1·21	96·81	0·83	98·36	1·02	98·77	1·32
Mg#			6·2	0·40			67·12	0·62	70·18	0·37	62·56	1·38	68·96	0·84
mol %														
En							41·83	1·07	43·65	0·94	37·64	1·45	65·38	0·86
Fs							20·50	0·70	18·54	0·45	22·53	1·15	29·43	0·81
Wo							36·98	1·65	37·18	1·36	38·97	2·12	4·19	0·41
An					52·66	2·48								
Ab					46·10	2·50								
Or					1·24	0·75								

	olivine	SD	olivine	plag	SD	opx	SD	pig	SD	pig	SD	diopside	SD	diopside	SD
n:	3		1	25		18		6		8		5		5	
SiO_2	35·84	0·09	34·02	44·89	1·00	50·60	1·12	52·53	0·90	50·56	1·01	51·26	0·26	50·39	0·37
TiO_2	0·04	0·04	0·00	0·03	0·03	0·28	0·09	0·23	0·07	0·56	0·16	0·46	0·03	0·65	0·10
Al_2O_3	0·01	0·01	0·00	33·36	0·51	0·66	0·15	0·73	0·26	1·98	0·42	2·81	0·34	2·87	0·12
MgO	30·82	0·56	35·62	0·09	0·21	19·01	0·47	20·99	0·91	19·22	0·86	15·04	0·26	13·94	0·31
CaO	0·23	0·09	0·15	17·82	0·54	1·84	0·18	3·92	0·52	7·74	1·15	21·26	0·29	20·34	0·20
MnO	0·75	0·13	0·82	0·03	0·04	1·02	0·19	0·74	0·08	0·69	0·18	0·13	0·13	0·13	0·10
FeO_{tot}	31·58	0·21	29·53	0·55	0·17	24·94	0·48	18·80	0·87	17·42	0·79	6·20	0·31	8·27	0·22
Na_2O	0·02	0·04	0·05	1·01	0·30	0·03	0·03	0·06	0·04	0·12	0·05	0·19	0·02	0·26	0·04
K_2O	0·02	0·02	0·00	0·02	0·02	0·01	0·01	0·03	0·03	0·03	0·02	0·01	0·01	0·01	0·02
P_2O_5															
Sum	99·5	0·3	100·3	98·1	1·2	98·5	1·6	98·9	0·7	98·4	1·2	97·7	0·4	97·2	0·6
Mg#						57·6	0·7	66·6	0·7	66·3	0·6	81·2	0·8	75·0	0·6
Mol %															
Fo	63·5	0·5	68·3												
En						54·5	0·9	60·4	0·7	55·0	1·9	44·4	0·5	41·9	0·5
Fs						40·1	0·6	30·3	0·8	28·0	0·9	10·3	0·5	13·9	0·3
Wo						3·8	0·4	8·1	0·9	15·9	2·5	45·1	0·7	43·9	0·4
An				90·6	2·7										
Ab				9·3	2·7										
Or				0·1	0·1										

*Composition of residual glass calculated by mass-balance (see text for details).
Bulk-rock analysed by inductively coupled plasma mass spectrometry. *n*, number of analyses; SD, standard deviation. FeO_{tot}, total iron reported as FeO. Fo (mol %) = 100[Mg/(Mg + Fe_{tot})] in olivine. En, Fs and Wo were calculated as in the study by Morimoto (1989). Mg# = 100[Mg/(Mg + Fe_{tot})]. An = 100[Ca/(Ca + Na + K)]; Ab = 100[Na/(Ca + Na + K)]; Or = [100K/(Ca + Na + K)]. End-members calculated as in the study by Deer *et al.* (1972). opx, orthopyroxene; pig, pigeonite.

within 0·0004 g of each other. This weight difference is about equal to the precision of the analytical balance, and confirms that no volatiles escaped during the experiments.

For each run, different XH_2O_{in} [= initial H_2O/($H_2O + CO_2$) in moles] were explored by means of adding different starting H_2O–CO_2 mixtures to the capsule so as to cover an XH_2O_{in} range of 1·00–0·12 (i.e. water-saturated to 'nominally' dry conditions; Table 3).

Experimental equipment

The experiments were conducted in a vertical internally heated pressure vessel (IHPV) pressurized with different mixtures of Ar + H_2 at room temperature to achieve the desired fO_2 conditions. A double-winding molybdenum furnace was used to achieve near-isothermal conditions (gradient <2–3°C) along a 3 cm long hotspot. Temperature was measured using three S-type thermocouples with an accuracy of ±5°C, whereas total pressure was recorded by a transducer with an uncertainty of ±20 bars. Typically, each experiment was loaded with a set of five basalt + H_2O + CO_2 charges plus one capsule containing a Ni–Pd–O or Co–Pd–O (depending on the desired fO_2; Taylor *et al.*, 1992) redox sensor, which was used to monitor the prevailing fH_2 at the desired T–P (Table 3). The set of capsules were run at
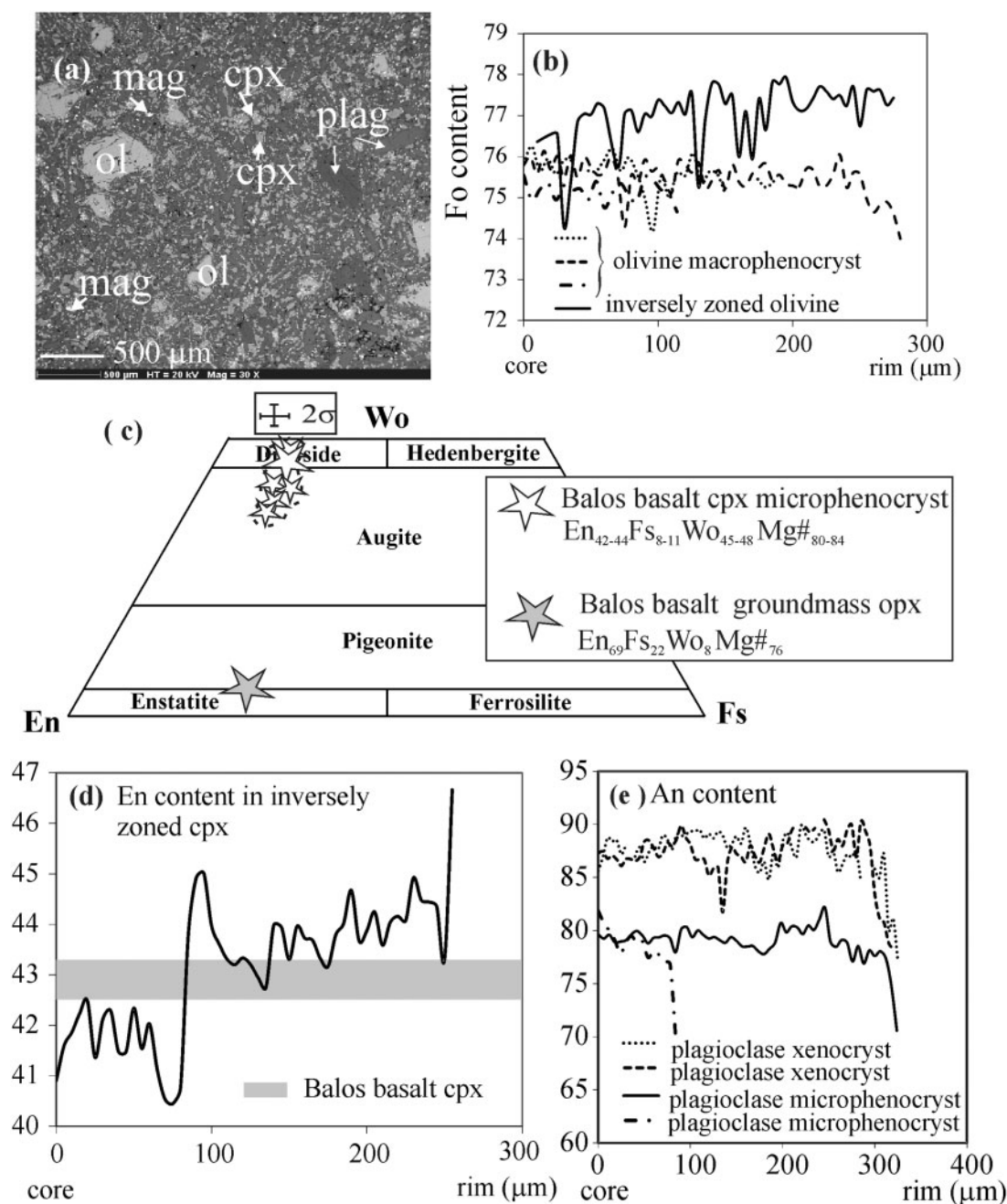
Fig. 2. Petrography and mineral chemistry of the Balos basalt sample. (a) Scanning electron microscope (SEM) image of the sample. ol, olivine; cpx, clinopyroxene; plag, plagioclase; mag, magnetite. (b) Core to rim compositional profiles for olivines. (c) Clinopyroxene phenocryst and orthopyroxene groundmass compositions plotted in the classification scheme of Morimoto (1989). The large white star shows the average composition of the cpx phenocrysts. (d) Compositional profile (core to rim) of a reversely zoned clinopyroxene. (e) Core to rim compositional profiles of plagioclase (microphenocrysts and xenocrysts).

the selected T–P–fH$_2$ for about 24 h, and experiments were terminated using a drop-quench device (Di Carlo et al., 2006). In all runs reported in Table 3 a rise in the total pressure was observed at the end of the experiment, showing that the sample holder had fallen into the basal cold part of the vessel, and that the drop-quench was successful (quench rate $> 100°C\,s^{-1}$). After the experiments, the capsules were checked for leaks, opened and some pieces of the run products were embedded in epoxy and polished for optical

observation, SEM imagery, back-scattered electron (BSE) identification and EMP analyses.

Water content, fH$_2$, fO$_2$ in the experimental charges

The procedure followed in this work for capsule preparation ensures fluid-saturated conditions for each charge. However, the relatively low amount of fluid phase used to minimize silicate dissolution into the fluid
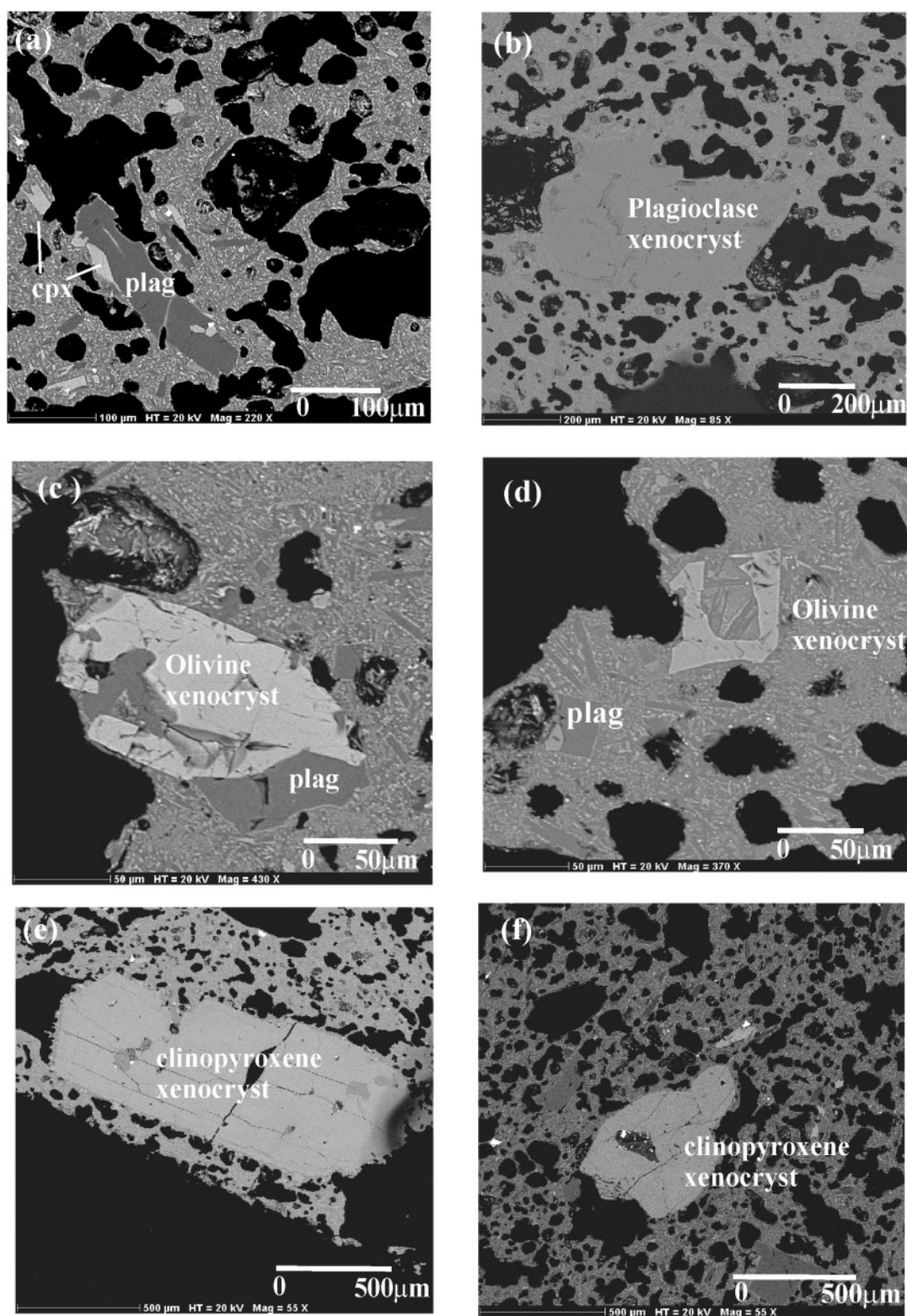
Fig. 3. Back-scattered electron images of the Upper Scoria 1 andesitic sample, showing (a) general view, (b) plagioclase xenocryst, (c, d) partially resorbed olivine xenocrysts, and (e, f) clinopyroxene xenocrysts.

resulted in the impossibility of obtaining direct measures of the final H_2O–CO_2 composition in the fluid phase. In addition, the majority of the charges were characterized by a high crystal content (>30 wt %;

Table 3), and homogeneous distribution of the mineral phases (see below), which (1) prevented direct H_2O determination by IR measurements and (2) made difficult the determination of water content using the
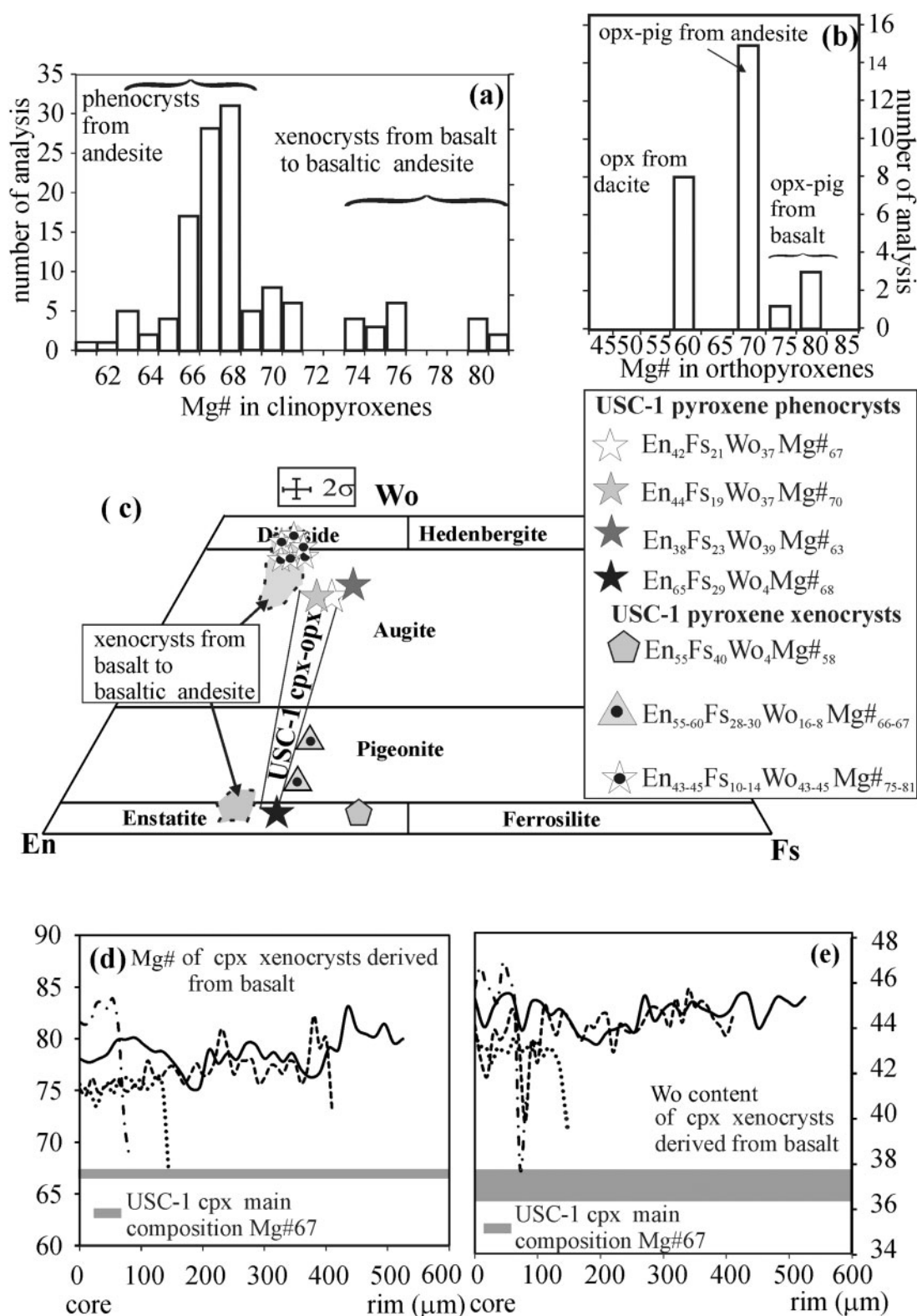
Fig. 4. (a, b) Histograms showing the populations of clinopyroxene and orthopyroxene present in the USC-1 andesite sample as functions of Mg#; the populations are labelled with interpretations discussed in the text; (c) compositions of clinopyroxene and orthopyroxene in USC-1, plotted onto the classification diagram of Morimoto (1989); tie-lines for the main cpx–opx populations are shown; those found in basaltic samples are also shown for comparison; (d) Mg# and (e) Wo content profiles across clinopyroxene xenocrysts in the USC-1 sample compared with the main andesite phenocryst composition (grey bands).
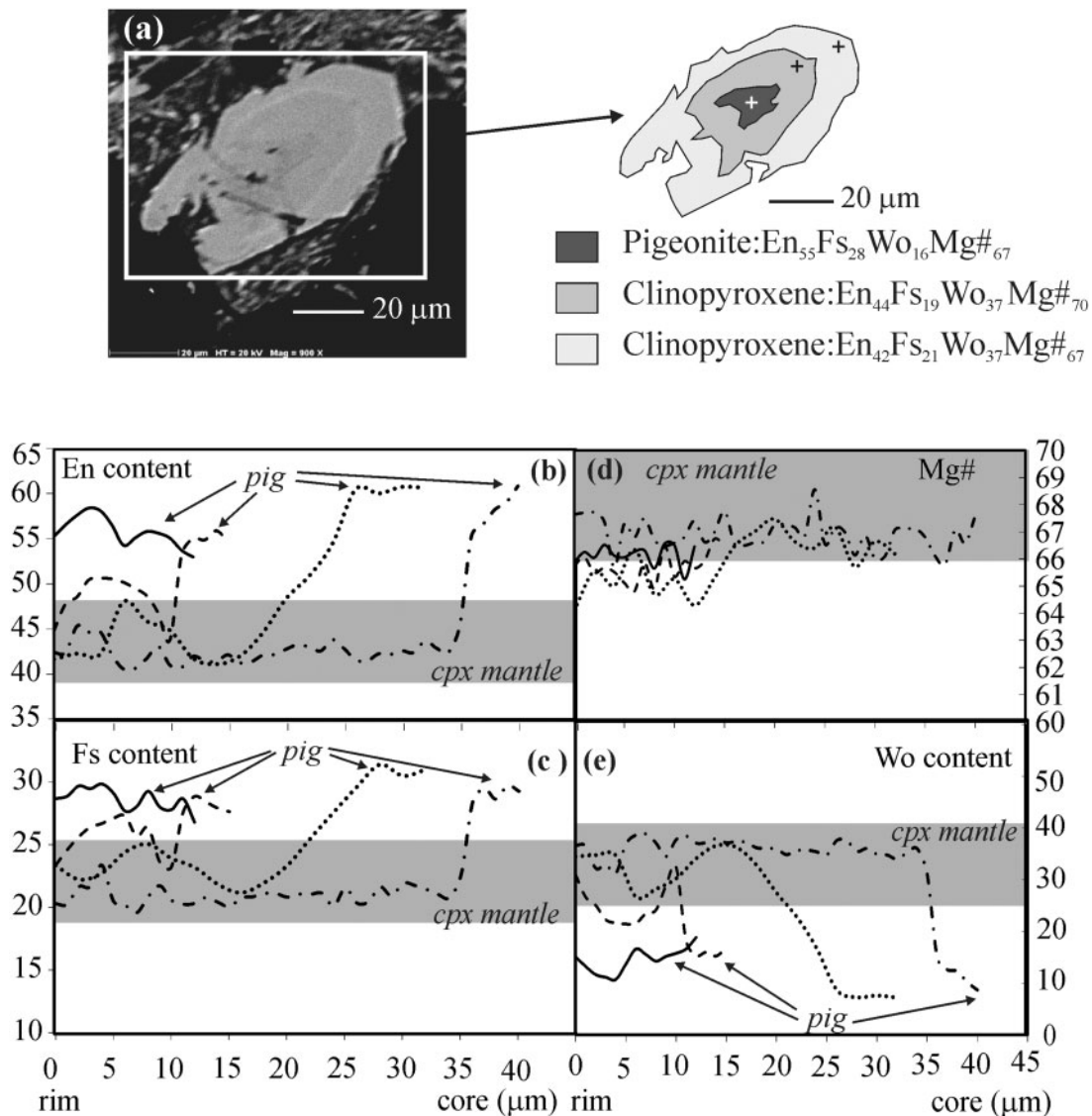
Fig. 5. (a) Back-scattered electron image of a pigeonite core mantled by normally zoned clinopyroxene (crosses show EMP analysis points); (b–e) rim to core compositional profiles of pigeonite from the andesitic USC-1 sample. (Note the cores mantled by clinopyroxene and the existence of isolated pigeonite crystals within the sample.)

'by-difference method' as this technique requires EMP analyses of residual glasses, which was not always possible owing to the high crystallinity of several charges (see below; Devine *et al.*, 1995). Thus, the H_2O_{melt} of each experimental charge under water-saturated conditions, and at a given *T–P*, was first calculated using the water-solubility model of Papale *et al.* (2006). The results thus obtained were used to calculate the $f°H_2O$ (fugacity of pure water at the relevant *P–T*) prevailing in these capsules by using the approach of Scaillet & Macdonald (2006). This approach uses an empirical equation of the form $f°H_2O$ (in bars) $= a(H_2O_{melt} \text{ wt \%})^b$, where the *a* and *b* parameters depend on magma composition. In our case, the fitted coefficients for the Balos basalt are $a = 50.053$ and $b = 1.995$. Then, for each H_2O-undersaturated charge (i.e. $XH_2O_{in} < 1$), the corresponding fH_2O was calculated using the relationship

$fH_2O = f°H_2O \times XH_2O_{in}$ (in moles), and the corresponding dissolved melt water content was retrieved using the relationship H_2O_{melt} (wt %) $= (fH_2O/50.053)^{1/1.995}$. We stress that this empirical calculation is equivalent to assuming ideal behaviour in the H_2O–CO_2 fluid phase and, hence, retrieved values must be considered as maximum water-dissolved contents (e.g. Berndt *et al.*, 2005; Andújar & Scaillet, 2012). Whenever possible, these results were compared with those obtained with the 'by-difference method', which were obtained from the summation deficit of the corresponding EMP analyses of residual glasses after alkali-migration correction (Table 3; see 'Analytical techniques' section below for more information concerning the alkali-migration correction). The results show that these two approaches agree within analytical error. Finally, the prevailing fO_2 of each charge was determined by knowing the intrinsic
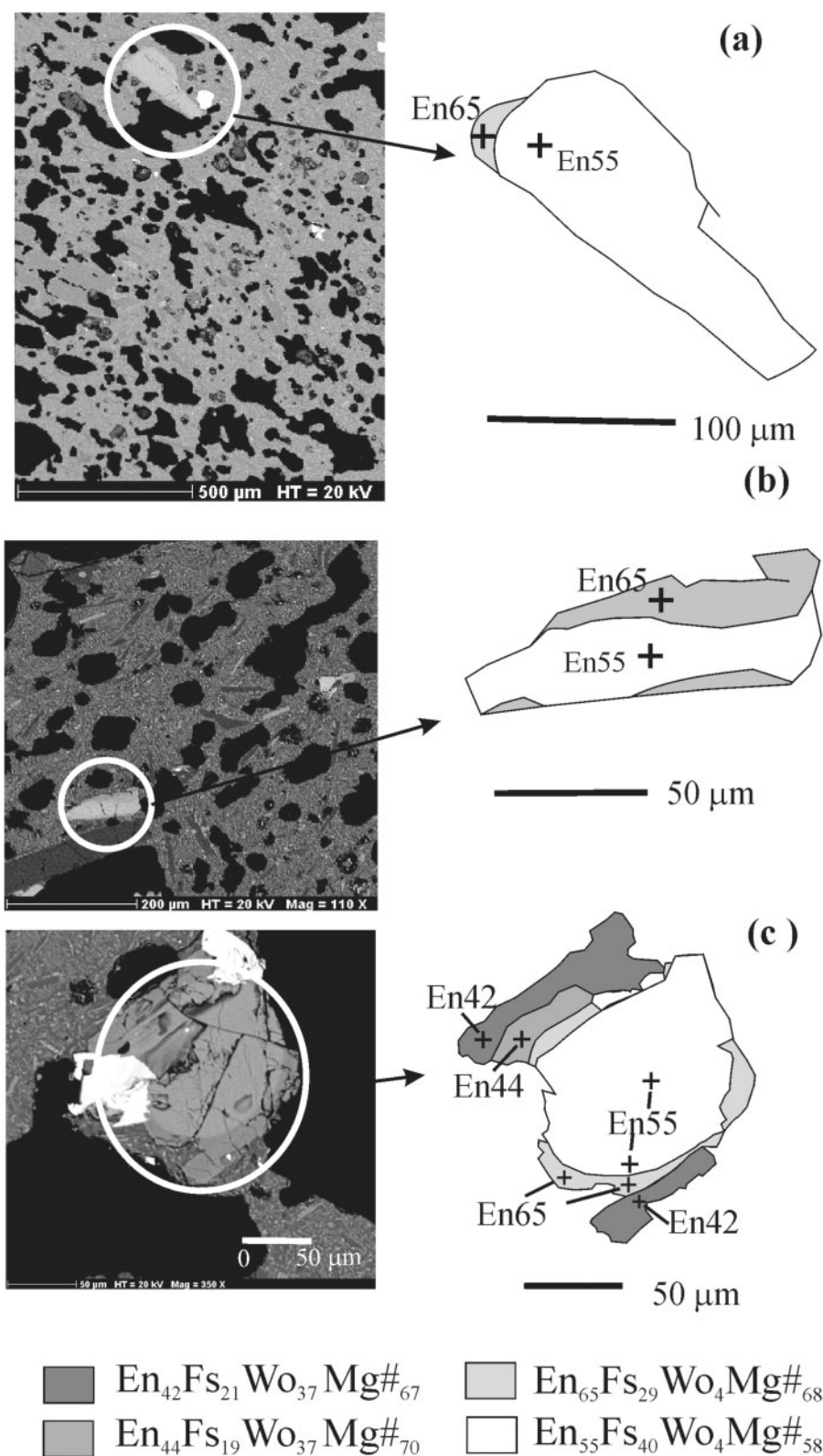
Fig. 6. Back-scattered electron images of orthopyroxene from the USC-1 andesitic sample. (a, b) Reversely zoned orthopyroxene; (c) reversely zoned orthopyroxene crystal mantled by normally zoned clinopyroxene (crosses show EMP analysis points).

fH$_2$ (obtained from the Ni–Pd–O and Co–Pd–O sensors), the dissociation constant of water (from Robie *et al.*, 1979), and the fH$_2$O of the charge at the experimental P–T calculated as explained above (i.e. Di Carlo *et al.*,

2006; Andújar & Scaillet, 2012). Results are given in Table 3. It is worth noting that, at each P–T–fH$_2$, the fO$_2$ varies with temperature and decreasing aH$_2$O (or XH$_2$O$_{in}$). Further details have been given by Scaillet
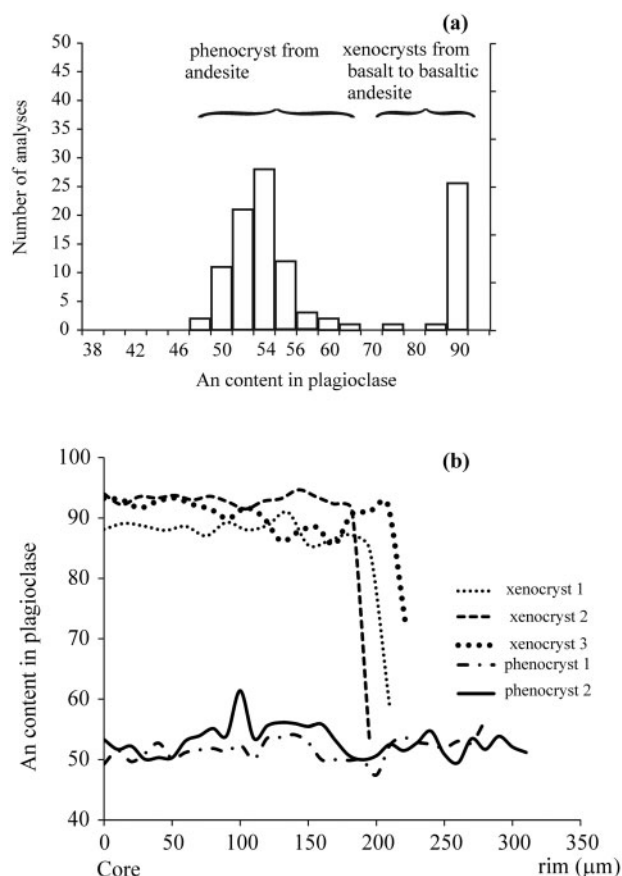
Fig. 7. (a) Histogram showing the populations of plagioclase found within the Upper Scoria 1 andesitic sample; (b) core to rim compositional profiles of USC-1 plagioclase (xenocrysts and phenocrysts).

et al. (1995), Freise et al. (2009) and Andújar & Scaillet (2012).

Experiments were performed in the range of temperatures 975–1040°C, but at two oxidation states: (1) under oxidizing conditions, with oxygen fugacities ranging from $NNO + 0.5$ to $NNO - 1.65$ (hereafter referred to as NNO experiments, NNO standing for the Ni–NiO solid reference buffer); (2) under slightly reducing conditions, in which fO_2 varied between $QFM + 0.6$ to $QFM - 3$ (hereafter referred to as QFM experiments, QFM standing for the quartz–fayalite–magnetite solid reference buffer). In addition, an extra set of experiments was conducted at highly oxidizing conditions at an $fO_2 \sim NNO + 3.5$ (Table 3).

Analytical techniques
Microprobe analyses were obtained with a Cameca SX-50 electron microprobe at ISTO-BRGM in Orléans, and with a JEOL JXA-8200 superprobe at the University of Huelva using an acceleration voltage of 15 kV, sample current of 6 nA, and a 10 s counting time. A focused beam was employed for analysing minerals, whereas a defocused 10 μm beam was used with glasses to minimize alkali migration (i.e. Morgan & London, 2005; Di Carlo et al., 2006). In addition, the crystal-free charge

s069-1 was analysed first in each probe session to quantify and correct the alkali effect with the 'by-difference' method for the determination of H_2O_{melt} in crystal-bearing runs.

Attainment of equilibrium
We performed only crystallization experiments in this study. As in previous similar studies (e.g. Freise et al., 2009; Pichavant et al., 2009, 2014), several observations demonstrate that near-equilibrium conditions were attained during the experiments: (1) the euhedral shape of the crystals; (2) the homogeneous distributions of phases within the charges; (3) the smooth variations of phase proportions and compositions with changes in experimental conditions; (4) the similarity of crystal–liquid exchange coefficients (K_d) of olivine, clinopyroxene and plagioclase to those from the literature calculated under similar conditions, which, in the case of olivine, also provides a test of the fO_2 determinations (see below; Pichavant et al., 2002); (5) the low residuals of mass-balance calculations (generally < 0.5; Table 3), which indicate that no major phase was omitted. Moreover, the run durations (≤ 24 h) are within the range of other studies performed on basaltic compositions for which near-equilibrium conditions have been also claimed (e.g. Di Carlo et al., 2006; Freise et al., 2009).

RESULTS

Mineral phases identified in the run products are olivine, clinopyroxene, magnetite, plagioclase, pigeonite, ilmenite and amphibole. Phase proportions were obtained by mass-balance calculation using the bulk-rock composition and the composition of the different phases present in the charge. The results are listed in Table 3 and displayed in a series of polybaric–isothermal or isobaric–polythermal diagrams showing the effects of T, P, H₂O content and fO_2 on phase relationships (Fig. 8). The position of the different mineral-in curves was first established based on the identified phase assemblages present in each charge and subsequently refined using phase proportions (Table 3).

Phase relationships at $fO_2 \sim$ NNO
At 200 MPa, under relatively oxidizing conditions (Fig. 8a) the phase assemblage is dominated by olivine, clinopyroxene, plagioclase and magnetite, liquidus conditions being reached at 1040°C for H_2O_{melt} slightly over 6 wt %. Amphibole crystallizes below 1000°C, being in a reaction relationship with both olivine and clinopyroxene in the water-rich part of the diagram ($H_2O_{melt} \geq 4$ wt %). At lower H_2O_{melt} amphibole is replaced by orthopyroxene. Orthopyroxene is stable only below 1000°C, where it is in a reaction relationship with olivine in the dry region (Fig. 8). At 200 MPa, an increase in fO_2 from $\sim NNO$ (Fig. 8) to $NNO + 3.5$ shifts orthopyroxene stability to higher temperatures (1040°C; Table 3); clinopyroxene and magnetite become the liquidus phases and crystallize before olivine whose crystallization interval

Table 3: Experimental run conditions and results

Run	$X\mathrm{H_2O_{in}}$ (moles)	$\mathrm{H_2O}$* (wt %)	$\mathrm{H_2O}$† (wt %)	log fO_2 (bar)	ΔNNO	ΔQFM	Ol	Cpx	Mag	Plag	Opx	Pig	Ilm	Amph	Crystal	Gl	$\sum r^2$
NNO experiments																	
1040°C, 200 MPa, 24.5 h, fH₂ (bar): 9.5 calc				−9.30	0.04												
s0968-1	1.00	6.30	5.95	−9.62	0.10										0.0	100.0	
s0968-2	0.75	5.45	7.43	−9.43	0.28		4.82	10.74	0.83	18.42					34.8	65.2	0.45
s0968-3	0.50	4.47	6.85	−9.42	0.29		4.52	11.81	0.12	24.21					40.7	59.3	0.38
s0968-4	0.34	3.65	5.93	−9.53	0.18		6.22	17.54	0.05	32.51					56.2	43.8	0.48
s0968-5	0.10	1.40	2.83	−10.31	−0.60		7.99	18.91	0.46	56.05					83.4	16.6	0.69
1000°C, 200 MPa, 27 h, fH₂ (bar): 9.73				−10.00	0.33												
s0968-6	1.00	6.30	5.94	−10.33	−0.04		4.09	16.70	2.40	29.66					52.8	47.2	0.25
s0968-7	0.67	5.16		−10.75	−0.53		X	X	X	X							
s0968-9	0.50	4.44	2.85	−11.10	−0.81		6.74	21.30	1.24	37.27					66.6	33.4	0.32
s0968-10	0.34	3.67		−11.65	−1.43		X	X	X	X							
s0968-11	0.10	1.40		—	—		X	X	X	X							
1040°C, 100 MPa, 28 h, fH₂ (bar): 6.11				−9.54	0.20												
s0968-12	1.00	4.30	6.63	−9.74	−0.01		4.46	14.11	0.49	20.33					39.4	60.6	0.22
s0968-13	0.70	3.60	6.30	−9.71	0.02		6.27	15.80	1.42	34.63					58.1	41.9	0.15
s0968-14	0.49	3.00	3.40	−10.41	−0.68		7.08	16.90	1.47	35.62					61.1	38.9	0.29
s0968-15	0.29	2.33	2.17	−11.38	−1.65		X	X	X	X							
s0968-16	0.10	0.96		—	—		X	X	X	X							
1040°C, 200 MPa, 31 h, fH₂ (bar): 0.2 calc				−5.98	3.73												
s0968-17	1.00	6.30	6.30	−5.98	3.73			12.67	3.29						16.0	84.0	0.23
s0968-18	0.72	5.35	4.55	−6.26	3.45		trace	22.30	4.55	36.60	2.09				65.5	34.5	0.21
s0968-19	0.52	4.52		−6.55	3.17			X	X	X	X						
s0968-20	0.33	3.63		−6.94	2.77			X	X	X	X						
s0968-21	0.10	1.40		−7.82	1.89												
975°C, 200 MPa, 23.5 h, fH₂ (bar): 4.50				−9.76	0.52												
s0968-22	1.00	6.30		−9.76	0.92				X	X			X				
s0968-23	0.71	5.31		−10.06	0.62		X	X	X	X			X				
s0968-24	0.52	4.55		−10.33	0.35		X	X	X	X			X				
s0968-25	0.33	3.62		−10.72	−0.05			X	X	X	X						
s0968-26	0.10	1.40		−11.41	−0.73			X	X	X	X						
1000°C, 400 MPa, 30 h, fH₂ (bar): 16.36				−9.77	0.56												
s0968-27b	1.00	8.98		−9.77	0.49		X	X	X	X							
s0968-28b	0.74	7.71	6.83	−9.86	0.39		7.64	13.08	0.99	27.10					48.8	51.2	0.09
s0968-29b	0.53	6.52	6.69	−9.94	0.31		9.65	18.67	1.12	30.73					60.2	39.8	0.08
s0968-30b	0.30	4.88		−10.09	0.13		X	X	X	X			X				
s0968-31b	0.10	2.00		−10.20	0.02		X	X	X	X			X				
QFM experiments																	
1000°C, 400 MPa, 28 h, fH₂ (bar): 33.32				−10.39	−0.06	0.46											
s0968-37	1.00	8.98		−10.39	−0.06	0.46	X	X	X								
s0968-38	0.69	7.44		−10.40	−0.07	0.45	X	X	X	X			X				
s0968-39	0.59	6.92	7.60	−10.45	−0.12	0.55	6.33	19.82	0.78	28.87			trace		55.7	44.3	0.05
s0968-40	0.29	4.82		−11.04	−0.71	−0.19	X	X	X	X	X	X	X				
s0968-41	0.10	2.00		−11.63	−1.30	−0.78	X	X	X	X	X	X	X				
1000°C, 200 MPa, 21 h, fH₂ (bar): 13.69				−10.29	0.04	0.55											
s0968-42	1.00	6.30	7.53	−10.41	−0.08	0.44	5.70	9.33	0.26	16.28					31.6	68.4	0.13
s0968-43	0.94	6.10	7.72	−10.36	−0.03	0.49	6.89	8.86	0.80	21.34					37.9	62.1	0.03
s0968-44	0.84	5.76	7.06	−10.44	−0.11	0.41	7.54	12.06	1.45	35.00			0.91		55.1	44.9	0.45
s0968-45	0.72	5.35		−10.80	−0.47	0.05	X	X	X	X			X				
s0968-46	0.54	4.63		−11.05	−0.72	−0.20	X	X	X	X			X				

(continued)

Table 3. Continued

Run	XH₂Oin (moles)	H₂O* (wt %)	H₂O† (wt %)	log fO₂ (bar)	ΔNNO	ΔQFM	Phase assemblage									
							Ol	Cpx	Mag	Plag	Opx	Pig	Ilm	Amph	Crystal	Gl	$\sum r^2$
975° C, 200 MPa, 24·5 h, fH₂ (bar): 53·54				−11·91	−1·58	−0·69											
s0968-32	1·00	6·30	7·10	−11·97	−1·26	−0·75	4·94	14·63	1·18	24·61				10·74	56·1	43·9	0·07
s0968-33	0·73	5·36		−12·26	−1·55	−1·04	X	X	X	X			X				
s0968-34	0·51	4·51		−12·84	−2·13	−1·62	X	X	X	X			X				
s0968-35	0·28	3·34		−13·91	−3·20	−2·69	X	X	X	X			X				
s0968-36	0·10	1·40		−14·50	−3·79	−3·28	X	X	X	X			X				
1040° C, 400 MPa, 23 h, fH₂ (bar): 26·86				−9·54	0·20	0·73											
s0968-47	1·00	8·98	6·48	−9·86	−0·12	0·41	1·31	8·56	0·49						10·4	89·6	0·67
s0968-48	0·70	7·54		−9·95	−0·21	0·32	X	X	X	X							
s0968-49	0·58	6·86		−9·97	−0·23	0·30	X	X	X	X	X	X					
s0968-50	0·30	4·92	4·77	−9·98	−0·24	0·29	11·88	20·20	1·29	43·01	trace	trace			76·6	23·4	0·18
s0968-51	0·10	2·00		−10·27	−0·53	0·00	X	X	X	X	X	X	X				
975° C, 400 MPa, 35 h, fH₂ (bar): 87·55				−11·55	−0·84	−0·33											
s0968-52	1·00	8·89		−11·66	−0·95	−0·44			X					X			
s0968-53	0·93	8·55		−11·72	−1·01	−0·50		X	X	X				X			
s0968-54	0·70	6·89	6·40	−11·92	−1·21	−0·75	10·65	18·88	trace	37·65				0·86	68·0	32·0	0·83

*Water content in the melt determined by the solubility model of Papale *et al.* (2006) using the method of Scaillet & Macdonald (2006).

†H₂O determined with the by-difference method (see text for details).

XH₂Oin, initial H₂O/(H₂O + CO₂) in the charge. fH₂ (bar), hydrogen fugacity of the experiment, determined using NiPd or CoPd alloy sensors; calc, calculated using the data obtained from successful NiPd or CoPd alloys (see text for details). log fO₂ (bar), logarithm of the oxygen fugacity calculated from the experimental fH₂. ΔNNO/ΔQFM, log fO₂ – log fO₂ of the NNO or QFM buffer calculated at *P* and *T* (NNO: Pownceby & O'Neill, 1994; QFM: Chou, 1978). Crystal content, values indicate the phase abundance in the charge (in wt %). Gl, glass; Ol, olivine; Cpx, clinopyroxene; Mag, magnetite; Plag, plagioclase; Opx, orthopyroxene; Pig, pigeonite; Ilm, ilmenite; Amph, amphibole; trace, phase with a modal abundance <0·1 wt %; X, phase identified using SEM.

is restricted to 5 wt % H₂O$_{melt}$ (Table 3), as observed in other experimental studies performed on basalt compositions under similar redox conditions (i.e. Parat *et al.*, 2014).

Phase relations at $fO_2 \sim$ QFM

The same assemblage occurs at near-liquidus conditions at 200 MPa and QFM (Fig. 8b). Amphibole is stable at H₂O$_{melt}$ > 5 wt %, where it crystallizes with olivine and clinopyroxene. Ilmenite is also present at H₂O$_{melt}$ < 6 wt %, whereas it is absent at NNO. Increasing pressure to 400 MPa at QFM produces a marked depression of the plagioclase-in curve, whereas ilmenite is no longer stable at H₂O saturation. Orthopyroxene (+ pigeonite) crystallizes at H₂O$_{melt}$ < 5 wt %, as also observed at 200 MPa and NNO; however, at these more reduced conditions (QFM) it persists up to 1040°C and co-crystallizes with olivine, which is not the case at NNO. The stability field of amphibole is broadly similar in shape to that at 200 MPa, this phase being in a down-temperature peritectic relationship with olivine and clinopyroxene.

The polybaric–isothermal section at 1000°C shows that orthopyroxene (+ pigeonite) reacts out between 400 and 200 MPa, for H₂O$_{melt}$ in the range 3–5 wt %, whereas olivine, clinopyroxene, magnetite (± ilmenite) remain stable under these conditions (Fig. 8d).

Phase proportions

The crystal contents of the experimental charges show a general increase with decreasing H₂O$_{melt}$, charges held at the same temperature displaying a near-linear inverse relationship with H₂O$_{melt}$ (see, for instance, the charges at 1040°C, 200 MPa). Liquidus conditions were attained at 1000°C, 200 MPa and 6 wt % H₂O$_{melt}$, whereas the highest crystal content (83 wt %) was reached at 1040°C, 200 MPa, NNO and 1·4 wt % H₂O$_{melt}$ (Fig. 9; Table 3). At constant temperature, H₂O$_{melt}$ and oxygen fugacity (i.e. 1000°C, QFM series), the general trend is to increase the crystal content with increasing pressure, an effect that is enhanced in the pressure range 200–400 MPa (Fig. 9). Magnetite, orthopyroxene and pigeonite are present in lower amounts (<3 wt %) compared with olivine and clinopyroxene. However, the proportion of Ca-poor pyroxene increases moderately with decreasing H₂O$_{melt}$ or temperature when compared with that of plagioclase, which rapidly becomes the dominant mineral (Table 3).

Phase compositions

Experimental phase compositions are reported in Supplementary Data Tables A4–A6 (supplementary data are available for downloading at http://www.petrology. oxfordjournals.org). Their variations with P–T–fO_2 and H₂O$_{melt}$ are discussed below.

Olivine

Olivine composition varies systematically with temperature, H₂O$_{melt}$, oxygen fugacity, degree of crystallization and melt composition (Fig. 10; Supplementary Data Table A1). In the range of explored *T*, *P*, *fO₂* and
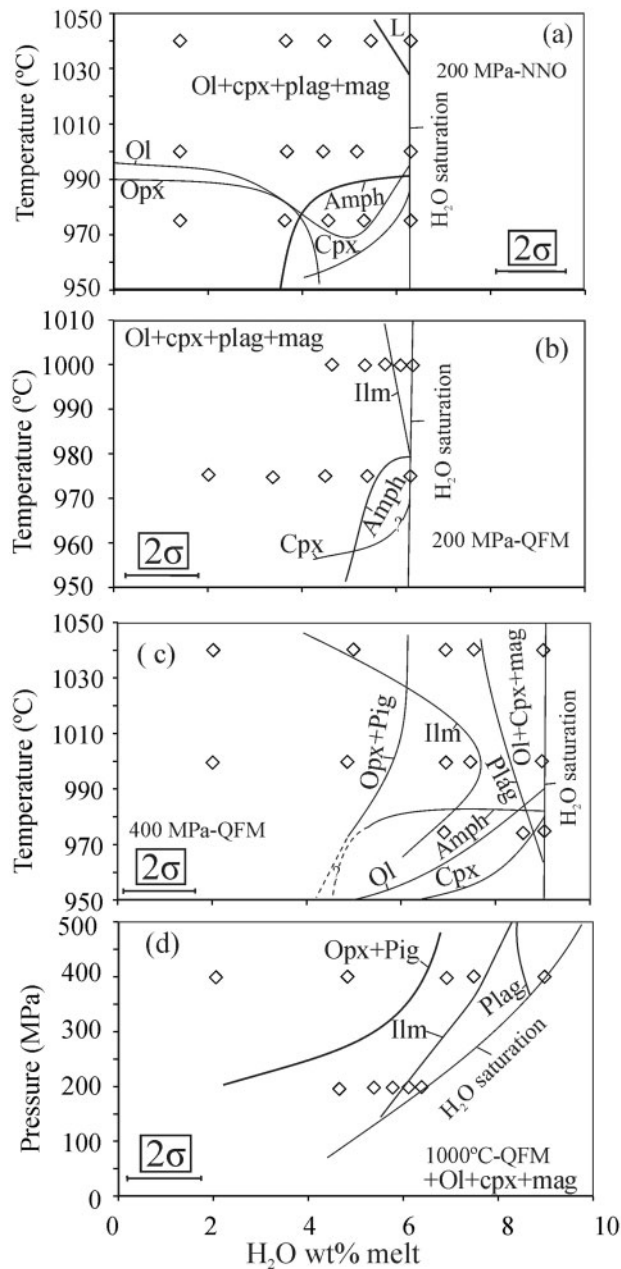
Fig. 8. Phase relationships of the Balos basalt at (a) 200 MPa and $fO_2 \sim$ NNO, (b) 200 MPa and $fO_2 \sim$ QFM, (c) 400 MPa and $fO_2 \sim$ QFM, and (d) 1000°C and $fO_2 \sim$ QFM, as a function of temperature, pressure and water content in the melt. ol, olivine; plag, plagioclase; cpx, clinopyroxene; opx, orthopyroxene; pig, pigeonite; amph, amphibole; mag, magnetite. Dashed lines are estimated phase boundaries. The tick on each phase boundary marks the side on which the phase is stable.

Fig. 9. Crystal content (wt %) vs H_2O_{melt} (wt %) for the experimental runs. Errors are equal to symbol size. Grey lines represent the 41 wt % total crystal content of the natural basalt (macrophenocrysts + microphenocrysts) and the 7 wt % macrophenocryst content (see text for details).

H_2O_{melt}, olivine composition varies between Fo_{91} and Fo_{64}. The highest Fo content (Fo_{91}) is reached at high fO_2 (NNO + 3·5) and at high temperature (e.g. 1040°C, 200 MPa, NNO + 3·5) whereas the lowest Fo content occurs at 1000°C, 400 MPa, QFM and 2·0 wt % H_2O_{melt}. At a given pressure, the Fo content decreases with decreasing H_2O_{melt} and temperature. At near-liquidus conditions, an increase in fO_2 increases the Fo content, in particular at 400 MPa and high H_2O_{melt} (9 wt %), where

Fo decreases by about 15 mol % from NNO to QFM (compare also the runs at 1040°C, 200 MPa, either at NNO or at NNO + 3·5, Fig. 10a). In general, at a given temperature and H_2O_{melt}, an increase in pressure decreases the Fo content [i.e. compare the run at 1000°C, 200 MPa, NNO with that at 1000°C, 400 MPa, NNO (Fig. 10a), the latter being displaced downward by 10 mol % Fo relative to the former]. In detail, the pressure effect on olivine composition remains modest in the pressure range 100–200 MPa at 1040°C, and is more significant in the range 200–400 MPa at 1000°C and 975°C.

As observed in previous studies, olivine composition varies with melt composition, and hence with the degree of crystallization (e.g. Berndt *et al.*, 2005; Di Carlo *et al.*, 2006). The Fo content decreases with the CaO/Al_2O_3 ratio or Mg# of the coexisting melt, both parameters being used here as indices of melt evolution (e.g. Pichavant *et al.*, 2002; Di Carlo *et al.*, 2006) (Fig. 10). Olivine becomes systematically richer in Fe as the proportion of clinopyroxene increases relative to olivine, and the coexisting melt becomes depleted in Mg and to a lesser degree poorer in Fe (Fig. 10b; see below for glasses; Table 3). The more Fe-rich olivines occur in H_2O_{melt}-poor charges (i.e. with the lowest melt fraction) in which plagioclase predominates over clinopyroxene and olivine (Table 3, Figs 9 and 10; Di Carlo *et al.*, 2006; Pichavant *et al.*, 2009). Notwithstanding, we should keep in mind
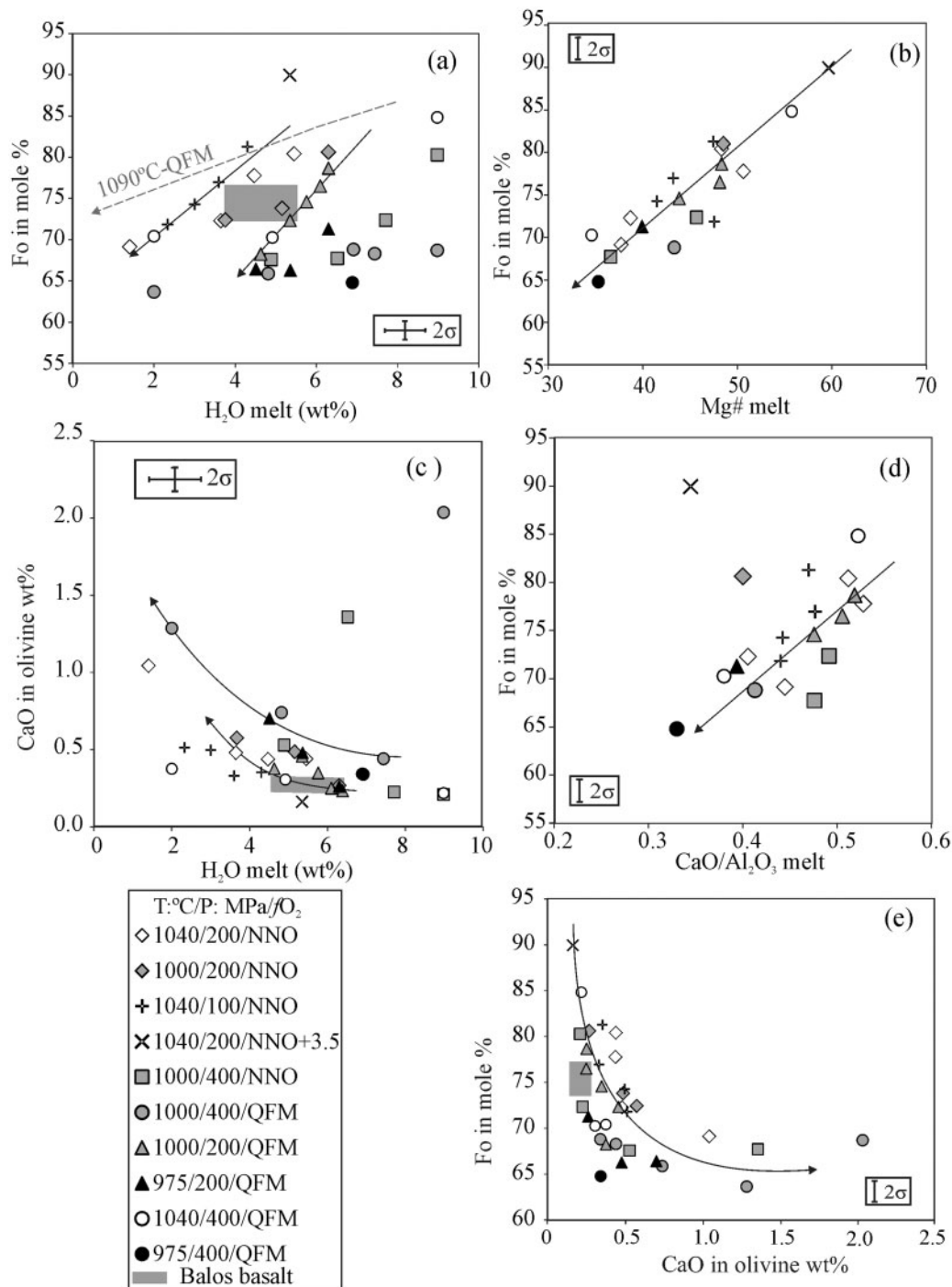
Fig. 10. Compositions of experimental olivines (Fo content in mol %) vs (a) H_2O (wt %) in the coexisting melt and (b) Mg# number of the coexisting melt; (c) CaO (wt %) in olivine vs H_2O_{melt}. (d) Fo content in mol % vs CaO/Al_2O_3 ratio in the coexisting melt; (e) Fo content in mol % vs CaO (wt %) in olivine. Numbers next to the symbols in the legend indicate temperature (°C), pressure (MPa) and prevailing fO_2 conditions. Dashed grey line in (a) represents the calculated olivine composition using equation (1) for the natural basalt at 1090°C and QFM (see text for details). Arrows show the direction of compositional change with decreasing water content.

that in single experimental series performed at constant T and P, the decrease in H_2O_{melt} decreases the fO_2 of the charges (Table 3). This effect is superimposed on those arising from T and H_2O variations, although our data suggest that it is a minor one, in particular in crystal-rich charges. At constant T and P, the average water difference along a given experimental series is ~4–5 wt %

H_2O_{melt}, which produces a decrease of about 1–1·5 log units in fO_2 (Table 3). Such a decrease in H_2O_{melt} decreases the Fo content in most series by 10–15 mol % (Fig. 10a, Supplementary Data Table A1). In contrast, an fO_2 change of 1–1·5 log units in crystal-rich charges affects Fo in olivine by 2–6 mol % (compare trends obtained at 200 MPa, 1000°C at either NNO or QFM).

The CaO content of olivine is generally accepted as a faithful indicator of the degree of evolution of the melt (Libourel, 1999). At any given temperature, CaO in olivine increases with decreasing H_2O_{melt}, Fo content and CaO/Al_2O_3 ratio of the melt (Fig. 10c–e; Supplementary Data Table A1), in agreement with previous work (Berndt *et al.*, 2005; Di Carlo *et al.*, 2006). The average olivine–liquid exchange coefficient K_d^{Fe-Mg} olivine/liquid is 0.27 ± 0.04 when calculated with $FeO = FeO_{total}$, and 0.30 ± 0.04 when calculated with melt Fe^{2+}/Fe^{3+} estimated by the method of Kress & Carmichael (1991) (Supplementary Data Table A1), using the experimental fO_2. Although not proof, the similarity between the latter K_d values and those of other studies (0.28–0.33, Sisson & Grove, 1993*a*; 0.33, Pichavant *et al.*, 2002; Barclay & Carmichael, 2004) suggests that our calculated fO_2 values are in the correct range and supports the overall attainment of equilibrium in the charges.

Olivine compositional changes as functions of *T*, H_2O_{melt} and fO_2 have been parameterized using a linear least-squares fitting procedure. We have not considered adding a pressure term to this equation (or in other parameterizations presented later) owing to the limited range of *P* variation in our experiments. The following empirical equation has been derived:

$$Fo(mol\ \%) = 0 \cdot 1037 \times T(^\circ C) + 1 \cdot 7638 \times H_2O_{melt}(wt\ \%) \\ + 3 \cdot 0234 \times \Delta NNO - 38 \cdot 63(R^2 = 0 \cdot 96). \tag{1}$$

Equation (1) back-calculates experimental Fo contents to within ± 1.4 mol %. Owing to its empirical nature, we caution the use of such an equation (and all similar equations that follow) for compositions significantly different from those of the Balos basalt.

Clinopyroxene

Experimental clinopyroxenes are either augite or diopside with compositions in the range $En_{40-49}Fs_{7-23}Wo_{27-46}$ and Mg# 68–87 (Supplementary Data Table A2). Clinopyroxenes with the highest Mg# values (calculated using Fe_{tot}), highest TiO_2 (0.6 wt %) and lowest Al_2O_3 contents (3.5 wt %) are found at 1040°C, 400 MPa, FMQ and 9 wt % H_2O_{melt} and at 1040°C, 200 MPa, NNO + 3.5 and 3 wt % H_2O_{melt} (Fig. 11). It is noteworthy that, as observed for olivine, clinopyroxene composition is strongly correlated with H_2O_{melt} (and hence with crystal content or melt composition; Fig. 11a–c). At a given temperature, a decrease of H_2O_{melt} from 7 to 2 wt % decreases the Wo content by about 10 mol % (Fig. 11c). Clinopyroxene becomes progressively poorer in Al_2O_3 and richer in SiO_2 and TiO_2 with melt evolution (Fig. 11d and e), a trend already observed in other similar experimental studies (i.e. Pichavant & Macdonald, 2007). Changes in temperature, pressure or oxygen fugacity (from NNO to QFM) have comparatively smaller effects (<5 mol % of each end-member molecule). The K_d^{Fe-Mg} values of clinopyroxene–liquid pairs range

between 0.19 and 0.41 (mean value 0.28, calculated using Fe_{tot}), again in agreement with previous experimental studies conducted on similar compositions (Supplementary Data Table A2; Pichavant *et al.*, 2002; Berndt *et al.*, 2005; Di Carlo *et al.*, 2006). The K_d^{Fe-Mg} varies linearly with the Mg# of the melt [K_d $_{cpx} = (0.007\ Mg\#_{melt}) - 0.07512$, $R^2 = 0.76$; Fig. 11f], variations in fO_2, *T* or *P* having little effect on this parameter (e.g. Toplis & Carroll, 1995). The variation of Wo content with experimental variables can be parameterized using a linear least-squares procedure on the entire experimental dataset:

$$Wo\ (mol\ \%) = 0 \cdot 075 \times T(^\circ C) + 1 \cdot 7357 \\ \times H_2O_{melt}(wt\ \%) - 0\ 0 \cdot 0973 \\ \times \Delta NNO - 46 \cdot 7042(R^2 = 0 \cdot 93). \tag{2}$$

Equation (2) back-calculates observed Wo contents to within ± 1.1 mol %.

Orthopyroxene and pigeonite

At 200 MPa and NNO + 3.5, orthopyroxene composition is in the range $En_{87-83}Fs_{10-13}Wo_{3-4}$ and Mg# 90–87, whereas at NNO it is $En_{68}Fs_{25}Wo7$ and Mg# 74, and at QFM it is $En_{64-76}Fs_{20-29}Wo_{3-6}$ and Mg# 69–79 (Fig. 12; Supplementary Data Table A3). At 400 MPa and QFM pigeonite has the composition $En_{59-52}Fs_{21-26}Wo_{15-24}$ with Mg# 67–73. The effect of experimental variables on orthopyroxene and pigeonite composition is less clear than for clinopyroxene. A decrease of H_2O_{melt} decreases En and Mg#, and increases Wo content, although for pigeonite the variation of Wo content with H_2O_{melt} is less significant (Fig. 12d). Our dataset on the effect of fO_2 on orthopyroxene composition is limited, but it appears that, at constant H_2O_{melt}, a decrease in fO_2 from NNO + 3.5 to QFM – 2 (see Table 3 for the fO_2 of the charges) decreases En and Mg# and increases Fs, whereas Wo is not affected (Fig. 12). Such a positive relationship between fO_2 and Mg# has also been documented for most ferromagnesian silicates (see, for example, Dall'Agnol *et al.*, 1999; Scaillet & Evans, 1999).

Plagioclase

Plagioclase compositions (Supplementary Data Table A4) are shown in Fig. 13 as a function of H_2O_{melt}, ranging from An_{89} to An_{58}, the highest value being reached at 1000°C, 200 MPa and 6 wt % H_2O_{melt}, and the lowest at 1000°C, 400 MPa and 2 wt % H_2O_{melt}, both at QFM. At a given *T*, *P* and fO_2, both the Ab and Or contents increase with decreasing water content in the melt (hence also with increasing crystal content), in agreement with previous studies (e.g. Sisson & Grove 1993*a*, 1993*b*; Berndt *et al.*, 2005). At fixed *T*, H_2O_{melt} and fO_2, variations in *P* do not significantly affect plagioclase composition, except at 975°C and QFM, at which a pressure increase from 200 to 400 MPa decreases An by 15 mol %. In general, plagioclase crystallizing at higher fO_2 tends to be slightly less calcic than that at lower fO_2
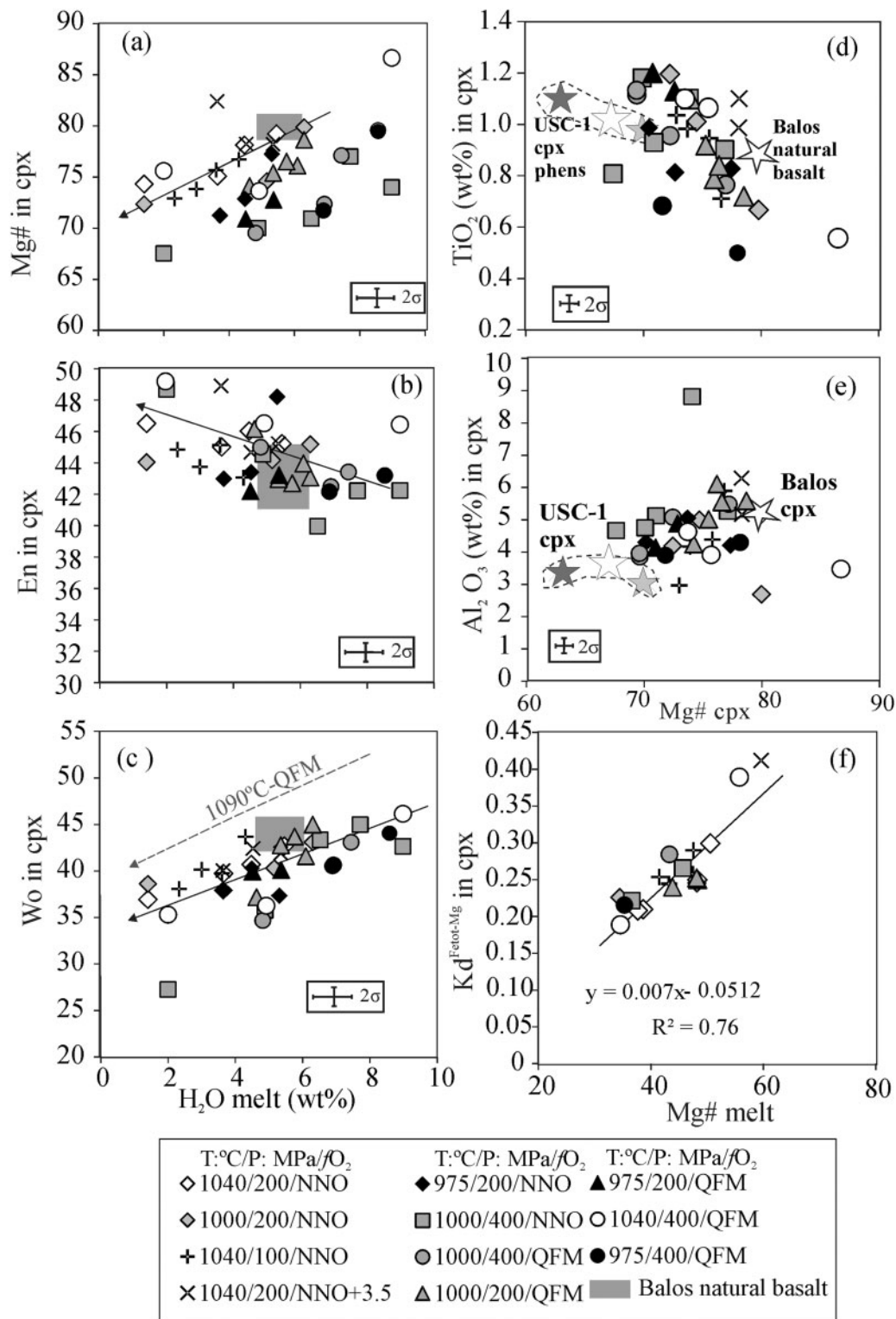
Fig. 11. Compositional variation of experimental clinopyroxene. (a) Mg#, (b) En content, and (c) Wo content of the clinopyroxene as functions of melt H_2O content. (d) TiO_2 (wt %) and (e) Al_2O_3 (wt %) contents as functions of Mg#. In (d) and (e) the stars show the cpx populations found in the Balos basalt and USC-1 andesite samples (legend as in Figs 2 and 4). (f) Fe–Mg crystal–liquid exchange coefficient for the experimental clinopyroxene vs Mg# of the melt. Numbers next to symbols in the legend indicate temperature (°C), pressure (MPa) and fO_2 conditions. Dashed grey line in (c) represents the clinopyroxene composition calculated for the natural basalt at 1090°C and QFM using equation (2) (see text for details). Arrows show the direction of compositional change with decreasing water content.
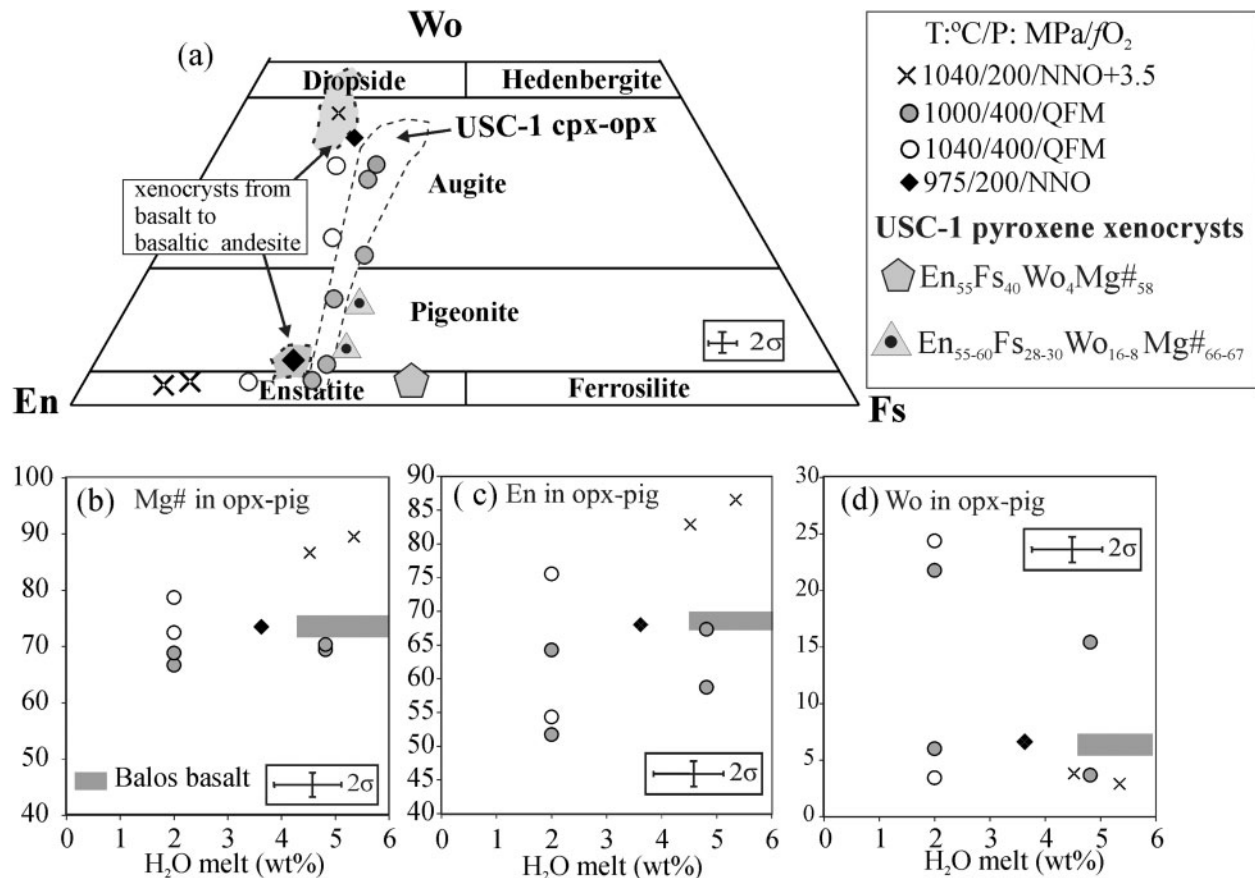
Fig. 12. Compositional variation of experimental pyroxenes. (a) Classification of experimental clinopyroxene, orthopyroxene and pigeonite. For comparison, we also show the cpx and pigeonite in the Balos basalt and the USC-1 andesite. (b–d) Variation of experimental opx–pigeonite Mg# (b), En content (c), and Wo content (d) vs H_2O_{melt}. Numbers next to symbols in the legend indicate temperature (°C), pressure (MPa) and prevailing fO_2 conditions.

(compare NNO and QFM runs at 200 MPa and 1000°C, Fig. 13). The plagioclase–liquid Ca–Na exchange K_d varies between 0·99 and 5·1 with a mean value of 2·23, in good agreement with previous studies on hydrous basaltic compositions (Baker & Eggler, 1987; Sisson & Grove, 1993a; Pichavant et al., 2002; Berndt et al., 2005; Di Carlo et al., 2006; Fig. 13; Supplementary Data Table A4). We have linearly regressed the compositional variations of plagioclase with T, H_2O_{melt} and fO_2, and obtained the following empirical equation:

$$An(mol \%) = 0 \cdot 279 \times T(°C) + 4 \cdot 623 \\ \times H_2O_{melt}(wt \%) - 2 \cdot 7982 \times \Delta NNO - 236 \\ \cdot 1693(R^2 = 0 \cdot 92).$$

(3)

The An content can also be regressed using the total crystal content instead of fO_2, yielding

$$An(mol \%) = -0 \cdot 0966 \times T(°C) - 0 \cdot 4015 \\ \times H_2O_{melt}(wt \%) - 0 \cdot 4799 \\ \times crystal content(wt \%) + 200 \\ \cdot 7324(R^2 = 0 \cdot 93).$$

(4)

Both equations retrieve observed plagioclase compositions to within ±1·4 mol %.

Amphibole

According to the classification of Leake et al. (1997) the experimental amphiboles are ferro-tschermakite to pargasitic hornblende in composition. The Mg# values of the experimental amphiboles (calculated with Fe_{tot}) show limited variability, with changes as functions of H_2O_{melt}, fO_2 or P (Fig. 14; Supplementary Data Table A5). In contrast, amphibole crystallizing at 400 MPa has a comparable, or even slightly higher, Al(IV) content than that crystallizing at 200 MPa, showing that any pressure effect on amphibole composition is minor in the 200–400 MPa interval (i.e. charges s0968-32 and s0968-54).

Fe–Ti oxides

The different Fe–Ti oxide phases present within the charges were recognized using BSE images. However, owing to their small size, microprobe analyses were generally contaminated by the surrounding glass, as indicated by the presence of variable amounts of K_2O and SiO_2. Fe–Ti oxide modal abundances are low (between 0·1 and 1·5 wt %) in runs conducted at $fO_2 \sim NNO–QFM$. Only in runs conducted at high fO_2
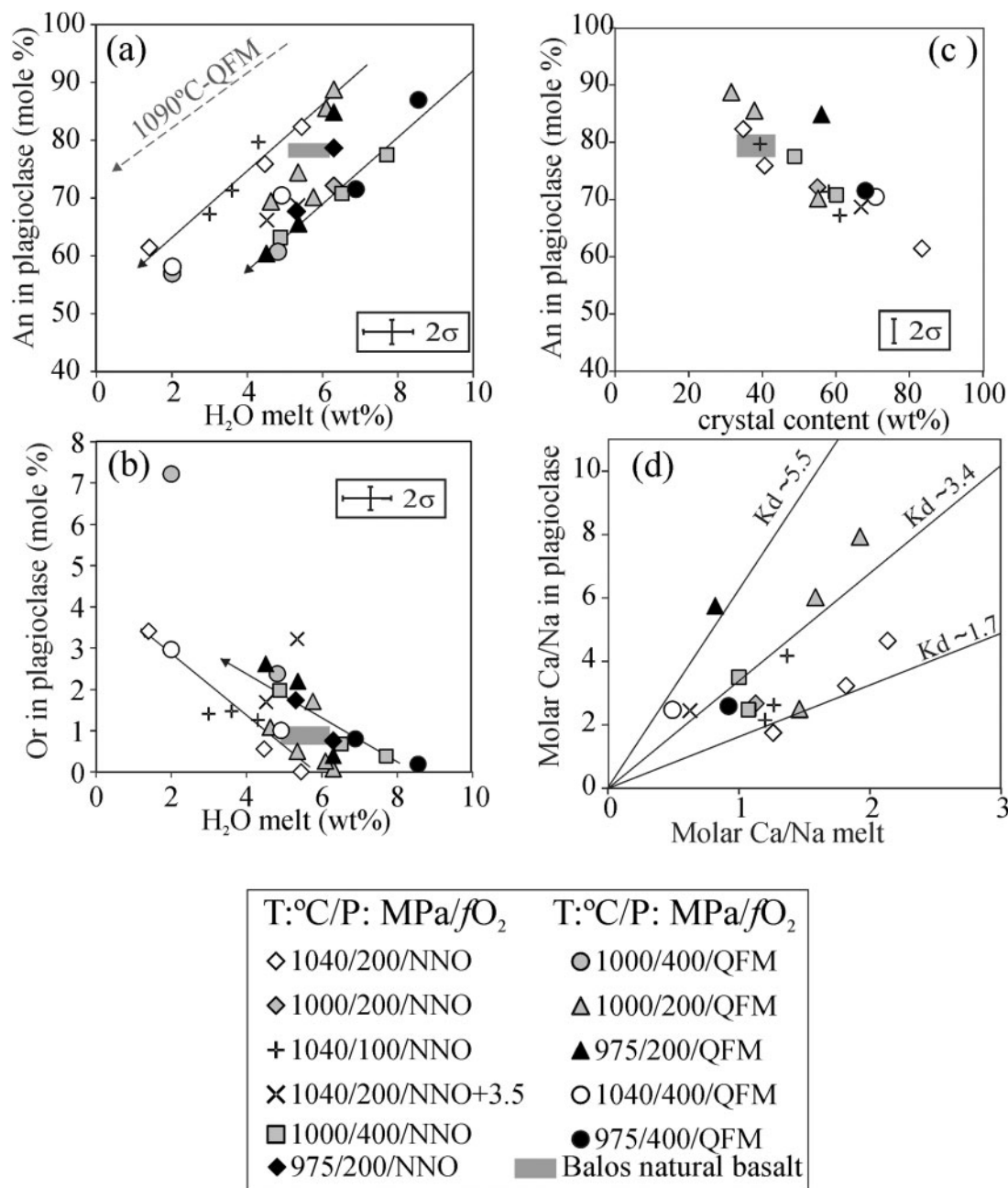
Fig. 13. Compositional variation of the experimental plagioclase. (a) An content (mol %) vs H_2O_{melt} (wt %); (b) Or content (mol %) vs H_2O_{melt} (wt %); (c) An content (mol %) vs crystal content (wt %); (d) Ca/Na in experimental plagioclase vs that in the coexisting melt. Lines show approximate K_d values from Sisson & Grove (1993a). Numbers next to the symbols in the legend indicate temperature (°C), pressure (MPa) and fO_2 conditions. Dashed grey line in (a) represents the calculated plagioclase composition for the natural basalt at 1090°C and QFM, using equation (3) (see text for details). Arrows show the direction of compositional change with decreasing water content.

(NNO + 3·5) do Fe–Ti oxide abundances exceed 3 wt % (up to 5·5 wt %, Table 3).

Experimental melts

Depending on the experimental conditions, the residual glasses range in composition from basalt to andesite, with only one charge (s0968-18; 1040°C, 200 MPa, NNO + 3·5, 5 wt % H_2O_{melt}) falling in the trachyandesite field (Le Bas & Streckeisen, 1991). SiO_2, K_2O, FeO_{tot} and

TiO_2 increase, and Al_2O_3, CaO and MgO decrease, with decreasing H_2O_{melt} (or increasing crystal content) (Fig. 15). This is a reflection of the crystallizing phase assemblage typical of arc magmas (olivine + clinopyroxene + plagioclase + spinel; e.g. Sisson & Grove, 1993a). At a given H_2O_{melt}, a decrease in temperature produces a decrease in FeO_{tot}, CaO and MgO contents and an increase in SiO_2, TiO_2, Na_2O and K_2O contents. FeO_{tot} remains almost constant for $H_2O_{melt} > 6$ wt %, but increases slightly at lower H_2O_{melt}
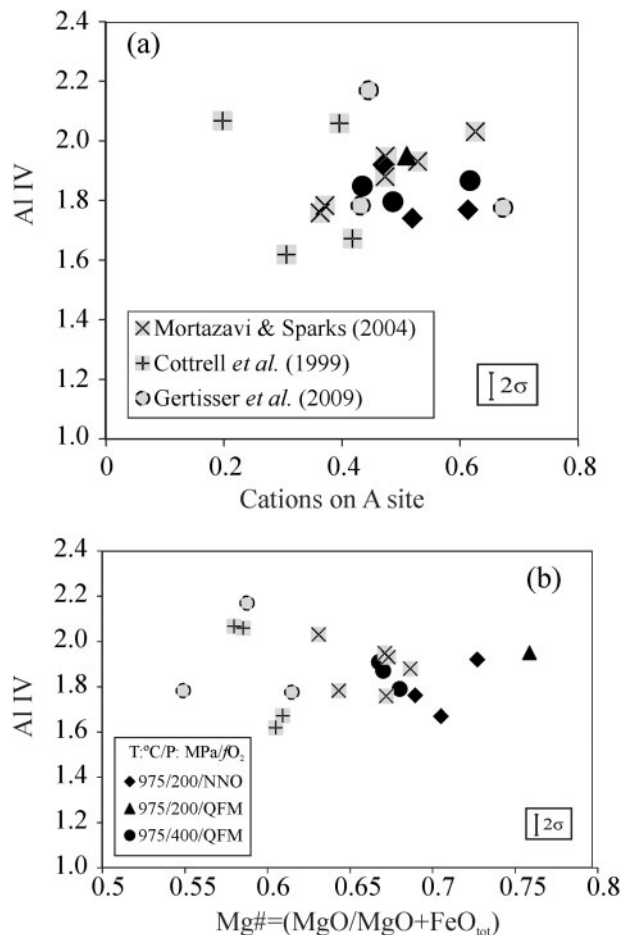
Fig. 14. Compositions of experimental amphibole (black symbols) compared with those from Santorini eruptive products (grey symbols). (a) Al(IV) vs cations on the A site; (b) Al(IV) vs amphibole Mg#. Structural formulae calculated in accordance with Leake *et al.* (1997). Numbers next to symbols in the legend indicate temperature (°C), pressure (MPa) and fO_2 conditions. Natural amphibole data are from Cottrell *et al.* (1999), Mortazavi & Sparks (2004) and Gertisser *et al.* (2009).

values. Experiments at $NNO + 3.5$ produced liquids with the lowest FeO_{tot} content, owing to profuse oxide crystallization. In contrast, a decrease in fO_2 from NNO to QFM does not produce significant changes in melt composition. This reflects the fact that (1) in almost all NNO and QFM charges the mineral assemblage is dominated by olivine, clinopyroxene, plagioclase ± magnetite (Table 3) and (2) the fO_2 values of the NNO and QFM series overlap to some extent (Table 3). The increase observed in FeO_{tot} and TiO_2 contents in runs carried out between $fO_2 \sim$NNO and QFM reflects the overall low amounts of crystallizing magnetite (<1·0 wt %) and the lack, or low abundance, of ilmenite. Only when the proportions of these phases exceed 1·5 wt % do the residual melts become FeO_{tot} depleted. The increase in pressure from 200 to 400 MPa does not produce significant changes in glass composition. However, decreasing pressure from 200 to 100 MPa at constant temperature produces residual melts enriched in SiO_2,

CaO and Al_2O_3 and depleted in FeO_{tot}, in particular at $H_2O_{melt} < 4$ wt % (Fig. 15).

DISCUSSION

Pre-eruptive conditions of the Balos basalt

Our experimental results can be used to constrain the P–T–H_2O_{melt} conditions under which the phenocryst assemblage of the Balos basalt was produced: olivine ($Fo_{74–78}$), plagioclase ($An_{72–80}$) clinopyroxene ($En_{43 \pm 2.6}$ $Fs_{11 \pm 1.2}Wo_{45 \pm 3.5}$, Mg# 80 ± 1.6), in addition to trace amounts of magnetite, ilmenite and orthopyroxene or pigeonite ($En_{69}Fs_{22}Wo_{7.8}$, Mg# 76). Coexistence of olivine–plagioclase–clinopyroxene–magnetite (Fig. 8) (macro- to micro-phenocrysts) broadly constrains the following P–T–H_2O_{melt} conditions: 980–1050°C, 100–400 MPa and 2–8 wt % H_2O_{melt}. This is admittedly a large domain, which reflects the large coexistence field of the ol + cpx + plag + mt assemblage (Fig. 8). The latter aspect precludes any fine tuning of pre-eruptive conditions using topological arguments alone. The lower temperature boundary of 980–1000°C, notably if H_2O-rich conditions prevailed (Fig. 8), is set by the lack of amphibole in the rock. Similarly, the lack of ilmenite in NNO charges, and its occurrence in those at QFM, indicates that fO_2 was probably close to the QFM buffer. At this fO_2, orthopyroxene is not stable at 200 MPa, whereas it occurs, along with ilmenite, at 400 MPa. Orthopyroxene has also been reproduced at 975°C, 200 MPa, 3·5 wt % H_2O_{melt} and $fO_2 \sim$NNO, but these conditions are too dry and cold to generate the observed plagioclase (An_{79}), clinopyroxene (Wo_{45}) and olivine (Fo_{75}) phenocryst compositions, and ilmenite is not present, unlike in the natural sample (Fig. 8a). Although orthopyroxene is not present as a true phenocryst in the basalt, it occurs as either isolated crystals or inherited cores in the andesite magma that is inferred to be generated by fractional crystallization of basalt (see below). Altogether, this suggests that andesite production from basalt took place within the stability field of orthopyroxene, and hence points to pressures around 400 MPa for basalt stagnation and production of andesitic derivatives (Fig. 8b; see below), and H_2O_{melt} not higher than 6 wt % (Fig. 8c).

Consideration of the main phenocryst compositions allows us to check the extent of crystal–liquid equilibrium. The variations of Fo (Fig. 10a), An (Fig. 13a) and Wo (Fig. 11c) contents with T and H_2O_{melt} show that the main phenocryst compositions (Fo_{75}, An_{79}, Wo_{45}) can be reproduced over a fairly wide range of melt water contents, depending on temperature. For instance, H_2O_{melt} contents of 3–4 wt % require a temperature of around 1040°C. For an H_2O_{melt} of 2 wt %, a temperature of 1090°C is implied [grey dashed lines in Figs 10, 11 and 13 obtained from equations (1)–(3)] whereas an H_2O_{melt} of 6 wt % requires a temperature at, or even slightly below, 1000°C. The same conclusion holds true for the crystal content, which is well reproduced under either set of T–H_2O_{melt} conditions (Fig. 9). Assuming
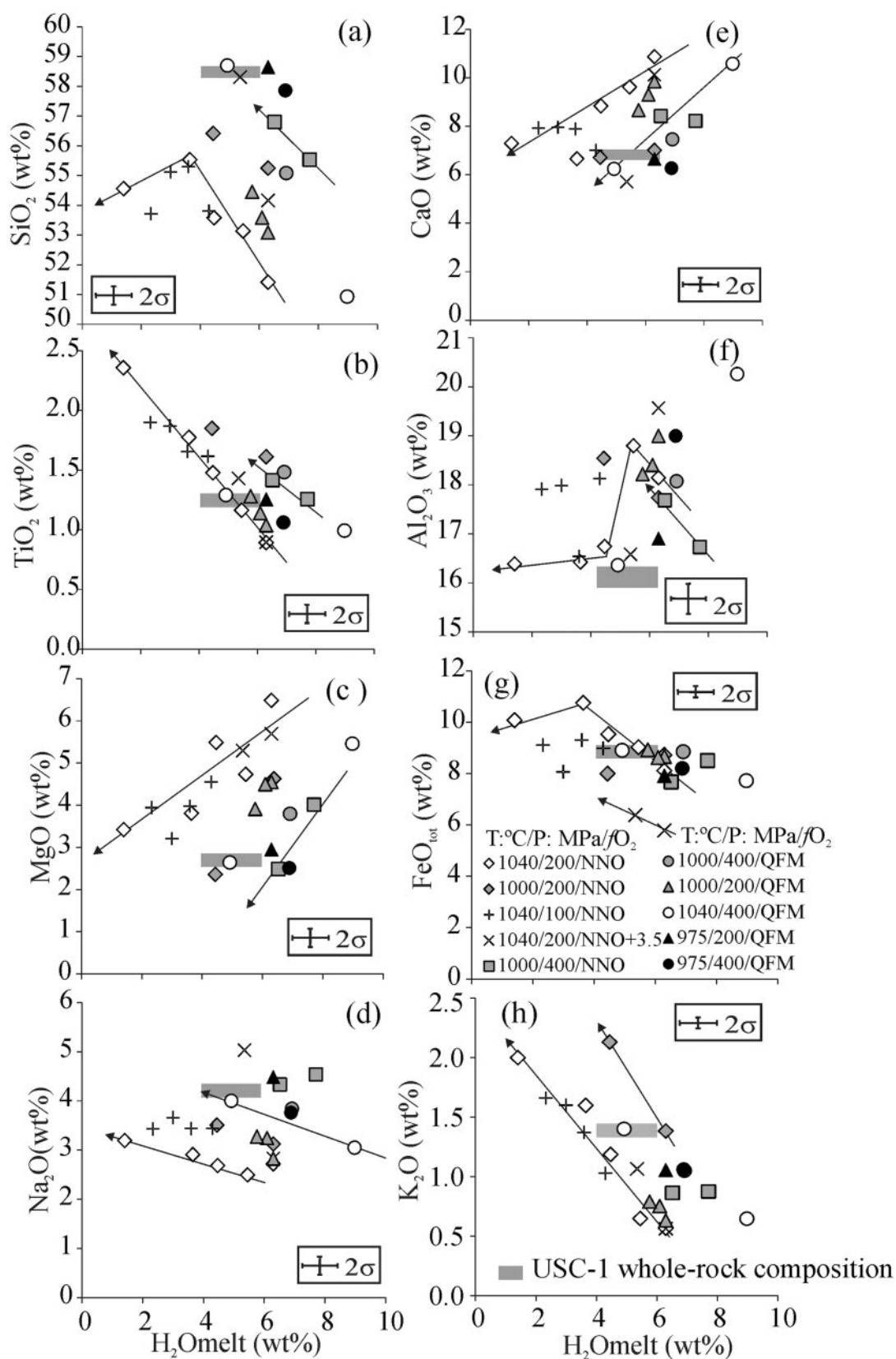
Fig. 15. (a–h) Experimental glass compositional variations of major and minor oxides with water content in the melt. Grey horizontal bar shows the natural USC-1 andesite bulk-rock composition. Arrows show the direction of compositional change with decreasing water content.

that only plagioclase and olivine are near-liquidus phases (on the basis of their greater abundances relative to clinopyroxene), together with an fO_2 near QFM (NNO – 0·7; see below), then solving simultaneously equations (1) and (3) (with Fo_{75} and An_{79}) yields $T = 1035°C$ and $H_2O_{melt} = 5$ wt %. Using these values as inputs in equation (4) yields a crystal content of 43 wt %, in good agreement with the estimated phenocryst content of the Balos basalt. Considering a phenocryst content of only 7–10 wt % would imply water contents >6 wt % (Fig. 9), which would be too high, however, to allow orthopyroxene crystallization by the time residual andesitic liquids are produced (see below). If clinopyroxene is included as a part of the main phenocryst assemblage, its Wo-rich character makes it difficult to avoid the conclusion that water-rich conditions prevailed, >5 wt % [equation (2), Fig. 11c]. The overall low CaO content of olivine (0·19 wt %, Table 1) is also more in accord with high H_2O_{melt} (Fig. 10c).

In summary, the pre-eruptive conditions of the Balos basalt are $fO_2 \sim QFM$ (based on ilmenite occurrence), $T > 1000°C$ (probably $1040 \pm 30°C$), 5–6 wt % H_2O_{melt}, and $P > 200$ MPa, possibly around 400 MPa. This indicates the water-rich character of the parent basalts at Santorini, a feature that has been already identified in similar volcanic suites from other locations (e.g. Sisson & Grove, 1993a; Pichavant *et al.*, 2002).

Origin of the Ca-rich plagioclase

The presence of Ca-rich $An_{90 \pm 1}$ plagioclase cores deserves further discussion. They are found in both the Balos basalt and USC1 andesite, displaying narrow rims that frequently match the composition of the main basaltic or andesitic plagioclase population. This shows that the cores resided long enough to partially equilibrate with the host melt prior to eruption (Figs 2 and 4). Similar calcic cores also occur within the more evolved silicic products (dacites, rhyodacites) and in mafic enclaves at Santorini (i.e. Nicholls, 1971a; Huijsmann *et al.*, 1988; Michaud *et al.*, 2000; Martin *et al.*, 2006; Gertisser *et al.*, 2009; Druitt *et al.*, 2012). Considering a basalt pre-eruptive H_2O_{melt} content of ~ 3 wt % at $\sim QFM$ using equation (3), a $An_{90 \pm 1}$ composition gives a temperature of $1110 \pm 5°C$ [and a crystal content of 10 wt % from equation (4)]. An H_2O_{melt} content of 4 wt % gives $T = 1095°C$ and a crystal content of 10 wt %. Such temperatures match well with homogenization temperatures obtained on melt inclusions trapped in An_{90} plagioclases and Fo_{80-76} olivines in Santorini basalts and gabbroic xenoliths ($1095 \pm 10°C$; Michaud *et al.*, 2000). Consequently, we suggest that such An-rich crystals grew from primitive, hot, mantle-derived melts that mixed (totally or partially) with basaltic to rhyodacitic liquids, during which they acquired Ca-poorer overgrowths matching the main plagioclase composition in the host magma. According to Nicholls (1971a) and Gertisser *et al.* (2009), mantle-derived magmas experience a first stage of crystallization or stagnation at

≥ 400 MPa, which may correspond to the An_{90} crystallization stage. Subsequently, such Ca-rich plagioclase-bearing melts rise to shallower levels (≤ 400 MPa) where they mix or mingle with pre-existing basaltic or more evolved melts. This mixing or mingling event may also be the source of the inverse compositional zonation observed in olivine and diopside from the basalt (Fig. 2).

Comparison with natural amphiboles

The comparison between the natural amphiboles in the mafic eruptive products from Santorini (Cottrell *et al.*, 1999; Mortazavi & Sparks, 2004; Gertisser *et al.*, 2009) and those from our experiments does not provide any constraints on the crystallization conditions of amphibole-bearing natural compositions owing to the considerable scatter of the natural data and the small compositional variation of the experimental phases (Fig. 14). Several thermobarometric methods based on the compositions of amphibole are available to define the crystallization conditions of amphibole-bearing magmas (i.e. Hammarstrom & Zen, 1986; Hollister *et al.*, 1987; Johnson & Rutherford, 1989; Schmidt, 1992; Ridolfi & Renzulli, 2012). Application of the Ridolfi & Renzulli (2012) formulation to the 400 MPa amphibole-bearing charges overestimates pressure by 75–140 MPa, and temperature by 40–100°C. In the 200 MPa experiments the pressure mismatch is even greater: the calculated values overestimate by 177–350 MPa the experimental ones (Supplementary Data Table A5). The Johnson & Rutherford (1989) calibration yields for all experimental amphiboles a pressure of ~ 500 MPa, whereas the Hammarstrom & Zen (1986), Hollister *et al.* (1987) and Schmidt (1992) models overestimate pressure by more than 200 MPa (Supplementary Data Table A5). The poor correlation between calculated and measured parameters is not surprising as our charges do not contain the buffering assemblage required for a proper use of Al-in-hornblende based barometers (Hammarston & Zen, 1986). However, the model of Ridolfi & Renzulli (2012) is thought to provide good constraints for rocks in which amphibole crystallizes at near-liquidus conditions (Martel *et al.*, 1999), which is not the case here. We conclude that care must be taken when applying the quoted thermobarometers to amphiboles hosted in mafic magma compositions [see also Erdmann *et al.* (2014) for further discussion].

fO_2 conditions needed for tholeiitic vs calc-alkaline trends

One of the most notable characteristics of the Santorini eruptive rocks is the compositional difference between old series products and the youngest volcanic rocks. Whereas volcanic products younger than 530 ka define a tholeiitic to weakly calc-alkaline trend, the earliest products (Early Centres of Akrotiri; 650–550 ka) have a more calc-alkaline affinity, and are depleted in FeO_{tot} and TiO_2, and enriched in CaO and MgO compared with
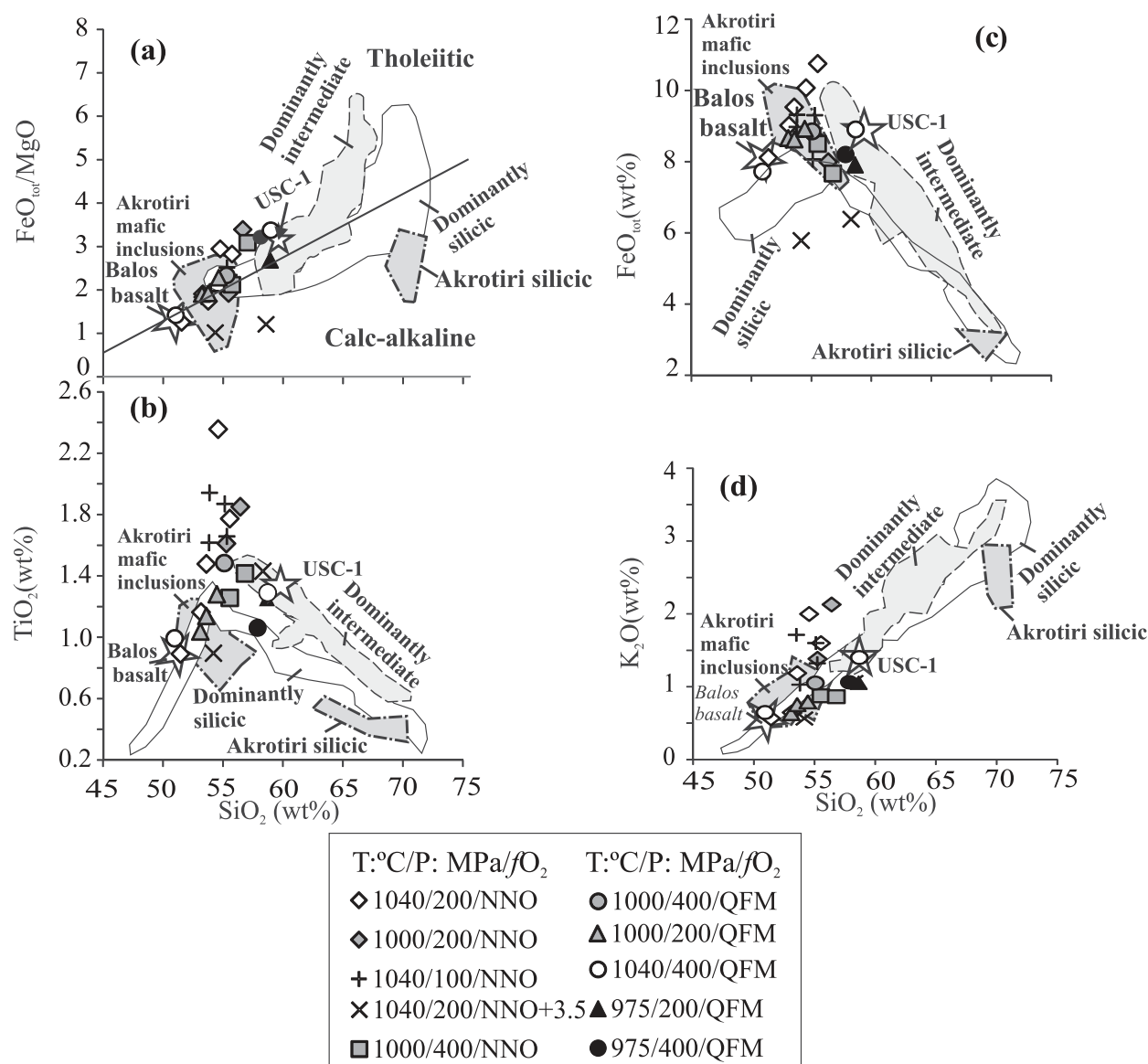
Fig. 16. (a) Tholeiitic vs calc-alkaline affinities of Santorini eruptive products (silicic and intermediate compositions) and experimental melts. (b) TiO_2, (c) FeO_{tot} and (d) K_2O variations vs SiO_2 (wt %) in the Santorini eruptive products compared with the experimental melts. Natural rock data from Druitt *et al.* (1999) and Mortazavi & Sparks (2004) for the Akrotiri series.

younger products. Such differences probably reflect temporal changes in the generation, evolution and/or storage conditions of the magmas (Nicholls, 1971*a*; Huijsman *et al.*, 1988; Druitt *et al.*, 1999; Mortazavi & Sparks, 2004).

Our experimental results can shed light on the mechanisms controlling the calc-alkaline vs tholeiitic affinity of magmas at Santorini. Experimental liquids produced by crystallization of the Balos basalt define different differentiation trends depending on the prevailing oxygen fugacity. Residual melts obtained at NNO and QFM show a FeO_{tot}/MgO ratio enrichment with increasing SiO_2, whereas liquids from experiments conducted at $fO_2 \sim NNO + 3.5$ display much lower FeO_{tot}/MgO values that do not vary with melt evolution (see Pichavant *et al.*, 2002). As discussed above, this is due to a combination of factors: (1) differences in the crystallizing

mineral assemblage; (2) changes in the relative proportions of plagioclase and Fe–Mg-bearing minerals; (3) the compositions of these phases. At NNO–QFM, the ratio of plagioclase to Fe–Mg minerals increases with decreasing water content, whereas the modal proportion of oxides remains low (Table 3). This drives the liquids toward higher silica and iron contents, coupled with a moderate increase in alkalis, generating a tholeiitic differentiation trend (Miyashiro, 1974; Sisson & Grove, 1993*a*; Berndt *et al.*, 2005). At high fO_2 ($>NNO + 1$) the crystallization of magnetite (>3 wt %) and Fe–Mg minerals in proportions similar to that of plagioclase, in particular at high H_2O_{melt} and temperatures (Table 3), results in early iron depletion and silica enrichment of the melt (Figs 15 and 16), yielding a typical calc-alkaline liquid line of descent (Miyashiro, 1974; Sisson & Grove, 1993*a*; Pichavant *et al.*, 1999; Berndt

et al., 2005). Thus, our results suggest that changes in prevailing fO_2 could control the calc-alkaline vs tholeiitic character of the erupted magmas at Santorini, the Akrotiri magmas being on average more oxidized than the younger ones. This is also supported by the Fe-depleted character of the Akrotiri products and the high Fe–Ti oxide contents of mafic enclaves from Akrotiri (4–9%; Mortazavi & Sparks, 2004).

Parameters controlling the differentiation trend of basaltic magmas during the early stages at Santorini

Andesitic magmas younger than 530 ka at Santorini have been discharged mainly as large andesitic ignimbrites (compare Upper Scoria 1), in small inter-plinian explosive eruptions, and as lavas (Nicholls, 1971*a*; Druitt *et al.*, 1999). These recent andesites have tholeiitic to weakly calc-alkaline affinities. Andesites also occur as minor components in the products of the large silicic plinian eruptions. Some of these have more calc-alkaline affinities, owing in part to magma mixing between basaltic and silicic components [being, however, less abundant than their fractionated tholeiitic counterparts in the recent products; see above and Druitt *et al.* (1999)]. The general trend within Santorini volcanic rocks is of increasing Al_2O_3, Na_2O and K_2O and decreasing MgO and CaO with increasing SiO_2 (Druitt *et al.*, 1999), as in our experiments. In detail, FeO_{tot}, TiO_2 and Al_2O_3 contents increase with differentiation until rock compositions reach *c.* 55 wt % SiO_2 (basaltic andesite), after which these oxides decrease (andesites; Fig. 16), reflecting the incoming of plagioclase and Fe–Ti oxides in the crystallization sequence. Overall, the Santorini rock series is well reproduced by our experimental melts, which shows that the explored $P–T–fO_2–H_2O$ conditions correctly simulate the natural context.

Residual andesitic liquids with ~58 wt % SiO_2 have been generated by 60–80 wt % crystallization from basaltic parents with 4·5–6·5 wt % H_2O_{melt} at QFM, 200–400 MPa and 975–1040°C (Tables 3 and Supplementary Data Table A6). The relatively modest change of melt composition with experimental parameters (T, P, H_2O melt, fO_2) makes it difficult to infer the conditions of subsequent melt evolution (i.e. after the production of andesitic melt). The variation of FeO_{tot}/MgO, TiO_2 and K_2O with increasing SiO_2 provides, however, some guidance in this respect. On a plot of FeO_{tot}/MgO vs SiO_2, experimental melts produced at NNO–QFM generally straddle the dividing line between calc-alkaline and tholeiitic fields and low-K–medium-K series, lying either within the field of Santorini magmas or slightly above them as fractionation proceeds (Fig. 16a). The only exception are the low-temperature melts, which fall onto the dividing line (at 975°C). In contrast, melts produced at NNO + 3·5 fall clearly outside the field of Santorini magmas. This suggests that the range of redox states explored experimentally brackets the redox conditions of Santorini magmas, and that the redox conditions of the natural system must lie towards

the reduced end of the explored spectrum (i.e. close to QFM-NNO). The plot of TiO_2 vs SiO_2 allows a more precise evaluation of fO_2 (Fig. 16b). On the one hand, experimental melts produced at NNO overshoot the curved natural trend of TiO_2 vs SiO_2 toward higher values, as a result of ilmenite not being stable (an effect that is well seen in charges conducted at NNO, 100 and 200 MPa, Fig. 16b). QFM melts, on the other hand, mimic well the observed inflection of TiO_2 content at around 57 wt % SiO_2 (Fig. 16b), owing to the onset of ilmenite crystallization under these redox conditions. This suggests that redox conditions around QFM and a pressure of 400 MPa are more appropriate for generating Santorini andesitic magmas than NNO, as also inferred for the Balos basalt. The degree of overlap between experimental and natural melts observed on plots of FeO_{tot} or TiO_2 vs SiO_2 or K_2O vs SiO_2 corroborates this hypothesis (Fig. 16c and d), as do fO_2 estimates obtained from coexisting magnetite–ilmenite pairs in the younger products (Gertisser *et al.*, 2009; Cadoux *et al.*, 2014; Druitt, 2014).

Our results demonstrate that basaltic andesitic to andesitic liquids at Santorini can be generated by 60–80 wt % crystallization of a Balos-type parental basalt at temperatures of 975–1040°C and with H_2O_{melt} contents in the range 3–6·5 wt %. Our results also show that andesitic melts can be generated over a range of pressures, which precludes, at this stage, any conclusive statement concerning the depth of andesite generation at Santorini. However, the comparison made below between our experimental results and the phase assemblage and mineral compositions of the USC-1 andesite sheds some light on this aspect.

Conditions of andesitic liquid generation at Santorini

Our petrographic study of the Upper Scoria 1 andesite has allowed us to recognize different mineral populations within the rock. The main phenocryst assemblage comprises plagioclase (An_{53}), augite ($En_{42}Fs_{21}Wo_{37}$, Mg# 67), orthopyroxene ($En_{65}Fs_{29}Wo_4$, Mg#68) and magnetite, which we consider to have crystallized from the host andesitic melt. Xenocrysts from a more mafic magma include partially resorbed olivine (Fo_{68-64}), pigeonite ($En_{55}Fs_{28}Wo_{16}$, Mg#66 to $En_{60}Fs_{30}Wo_8$, Mg#67), high-Ca plagioclase (An_{91-89}), and diopside ($En_{43-45}Fs_{10-14}Wo_{43-45}$, Mg#75–81), but also reversely zoned orthopyroxene ($En_{55}Fs_{40}Wo_4$, Mg#58), the core of which probably crystallized from a more evolved magma composition (i.e. dacite; see above) (Table 2; Figs 4–7).

To a first-order approximation the partially resorbed phenocryst minerals and mafic cores can be interpreted to reflect the conditions of generation of the Upper Scoria 1 andesitic liquid (excluding the An_{91-89} plagioclase, which may correspond to an earlier crystallization stage, as noted above). Thus, a first constraint on the melt generation conditions of USC-1 can be made by comparing the xenocrystic mineral assemblage of the

natural andesite with the basalt phase relationships determined here. The xenocrystic assemblage olivine, augite, plagioclase, orthopyroxene and pigeonite has been reproduced only at 300–400 MPa, QFM, $H_2O_{melt} < 6$ wt % and in the temperature interval 1040–990°C (Fig. 8c and d). It should be noted, however, that at such conditions trace amounts (<0·1 wt %) of ilmenite are present, but this is not found in the natural andesite (Fig. 8c).

As for the basalt, the compositions of the xenocrystic phases in USC-1 can be used to check and refine this estimate. Experimental olivines from charges annealed at QFM and 400 MPa reproduce the composition of the USC-1 xenocrystic olivines, in particular at 1000°C (Fo_{68-64}; Fig. 10a). For example, an average Fo_{66} olivine would imply an H_2O_{melt} content of 4–6 wt % in the basalt at 1000°C. The compositions of cpx–opx pairs crystallizing in experimental charges under these conditions clearly fall along the tie-lines defined by the USC-1 xenocrystic cpx–opx pairs (Fig. 12a). Moreover, the xenocrystic pigeonite and orthopyroxene in the USC-1 andesite are also broadly reproduced under the same conditions in the range $H_2O_{melt} = 2-4\cdot5$ wt %, although their more erratic compositional variations with T and H_2O_{melt} (Fig. 12) make them rather imprecise mineral indicators of intensive parameters. The USC-1 xenocrystic clinopyroxene has a Wo content of 43–45%, which also points to rather elevated H_2O_{melt}, in the range 5–7 wt % (Fig. 12d). Plagioclase crystallizing at 1000°C and 2–4·5 wt % H_2O_{melt} is An_{60-57} (Fig. 13a), similar to the calcic end-member of the andesite phenocryst population (Fig. 7a). Similarly, the composition of clinopyroxene crystallizing under the above conditions encompasses the Mg-rich pole of andesite phenocrysts ($En_{44-46}Fs_{19}Wo_{37}$, Mg#70; Fig. 11). Overall, the fact that the experiments at 400 MPa closely reproduce the xenocrystic assemblage and phenocryst compositions of USC-1 suggests that the USC-1 liquid was generated at 400 MPa, at around 1000°C and QFM, with ~4–6 wt % dissolved H_2O. Although we could not obtain the residual liquid composition of charges strictly matching those conditions, the residual melts of neighbouring (in *P–T–X* space) charges are sufficiently close to the USC-1 magma to support the likelihood of andesite generation from basalt crystallization, as illustrated in Fig. 16. The liquid compositional variations displayed in Fig. 15 show that melts produced at 1000°C and QFM generally fall close to a USC-1 type andesite, at either 200 or 400 MPa, in the H_2O_{melt} range 4–6 wt %. The main constraint on pressure arises from orthopyroxene and pigeonite stabilities (Fig. 8); these phases grew only at 400 MPa, suggesting this as the likely pressure of the reservoir for andesite production from basalt crystallization. A lower temperature limit of 975°C is provided by the necessity of not crystallizing amphibole in any significant quantity.

We conclude that andesite production at Santorini probably occurs in a mid-crust reservoir at around 400 MPa. Andesitic liquids are produced by 60–80 wt %

crystallization of a Balos-like basaltic parent, at a temperature of about 1000–1025°C, and with 4–6 wt % H_2O_{melt}. We stress that those conditions are not equal to the pre-eruption conditions inferred above for the Balos basalt, which are somewhat hotter. It is worth stressing that such conditions are similar to those inferred from detailed investigations of melt inclusions in mafic magmas associated with the Minoan eruption (Michaud *et al.*, 2000), thus lending credence to the general conclusion that the majority of the Santorini andesites are true liquids, with considerable amounts of dissolved water, which are derived from basalts by crystal fractionation processes (Nicholls, 1971*a*; Barton *et al.*, 1983; Mann, 1983; Huijsmans & Barton, 1989; Huijsmans *et al.*, 1989; Michaud *et al.*, 2000: Zellmer *et al.*, 2000). These residual liquids are inferred to separate from the parent basaltic mush to generate andesite-dominated eruptions such as USC-1. This separation from the gabbroic crystal residue could be facilitated by the low density and viscosity of the water-rich andesitic melts ($2\cdot3 \pm 0\cdot1$ g cm^{-3}, Bottinga & Weill, 1970; $2\cdot2 \pm 0\cdot4$ Pa s; Giordano *et al.*, 2008). In the case of USC-1, however, the crystal–liquid separation was imperfect, as a small but detectable proportion of the crystals in USC-1 can be demonstrated to originate from the gabbroic mush zone where the andesite was produced; such residual crystals were entrained along with the andesitic melts and served as preferential nucleation sites from which the dominant phenocryst assemblages grew (Fig. 5).

Comparison with the ancient series of Akrotiri

Magmas of the Early Centres of Akrotiri (650–550 ka) have calc-alkaline affinities, whereas the younger (<530 ka) Santorini magmas are weakly calc-alkaline to tholeiitic (Fig. 16a; Nicholls, 1971*a*; Druitt *et al.*, 1999). The Akrotiri eruptive rocks are also characterized by the presence of hornblende, which is rare in the younger deposits, suggesting at first sight that they evolved under more oxidizing and hydrous conditions than the younger magmas (Druitt *et al.*, 1999). According to our results, production of magmas with calc-alkaline affinities requires fractionation of basalt under oxidizing (>NNO and <NNO + 3·5; Fig. 16a) conditions. Within the range of pressures, temperatures and fO_2 explored in this study, amphibole is stable at ≤975°C and at $H_2O_{melt} > 3\cdot5$ wt % at $fO_2 \sim$ NNO, whereas under more reducing conditions amphibole appears only at $H_2O_{melt} > 5$ wt %. The generally amphibole-free magmas that typify Santorini volcanism since 530 ka therefore evolved under somewhat hotter (but not drier) and more oxidizing conditions than the early (650–550 ka) Akrotiri magmas (e.g. Mortazavi & Sparks, 2004), perhaps reflecting changes in magma source and magma fluxes.

CONCLUSIONS

Our experiments on the Balos basalt extend a recent phase-equilibria study of Santorini silicic magmas

([Cadoux *et al.*, 2014](#)) to more mafic compositions. Phase equilibrium experiments on a high-Al basaltic sample from the Balos cinder cone (344 ± 24 ka), combined with detailed petrological characterization of the natural Balos basalt, have allowed us to constrain the pre-eruptive storage conditions of mafic magmas at this volcano. Comparison of the experimental results with phase assemblages and compositions of a typical Santorini andesite (Upper Scoria 1 eruption; 80 ka) have also allowed us to estimate the conditions under which basaltic-andesite to andesitic magmas are generated. If the Balos basalt is representative of the average basalt feeding Santorini, then our results show it to be relatively rich in water. We estimate that Balos-like basalts are stored prior to eruption at 400 MPa, QFM, 5–6 wt % H_2O_{melt} and $T > 1000°C$ (1040 ± 30°C). They may either erupt to give Balos-like lava flows or crystallize further at depth to produce andesitic liquids. Comparison of our experimental results with the Upper Scoria 1 andesite suggests that production at 400 MPa of andesitic melts requires similar, albeit cooler, conditions (i.e. 4–6 wt % H_2O_{melt} at around 1000°C and QFM), andesitic melts being produced after 60–80 wt % crystallization of an ol + cpx + plag + Ti-mag + opx ± pig–ilm assemblage. The andesite thus produced has a relatively high water content, which may play a role in facilitating its extraction from the mafic mush (by decreasing liquid viscosity). Our results confirm previous suggestions that the calc-alkaline or tholeiitic character of Santorini magmas is controlled by changes in the prevailing oxidation state. However, it is remarkable that recent magmas, despite being more reduced, are not any drier compared with earlier more oxidized products (i.e. Akrotiri) at this volcanic centre. Hence there is no simple relationship between magma oxidation state and water content.

SUPPLEMENTARY DATA

[Supplementary data](#) for this paper are available at *Journal of Petrology* online.

REFERENCES

Andújar, J. & Scaillet, B. (2012). Experimental constraints on parameters controlling the difference in the eruptive dynamics of phonolitic magmas: the case of Tenerife (Canary Islands). *Journal of Petrology* **53**, 1777–1806.

Bachmann, O., Dungan, M. A. & Lipman, P. W. (2002). The Fish Canyon magma body, San Juan volcanic field, Colorado: rejuvenation and eruption of an upper-crustal batholith. *Journal of Petrology* **43**, 1469–1503.

Bacon, C. R. & Druitt, T. H. (1988). Compositional evolution of the zoned calcalkaline magma chamber of Mount Mazama, Crater Lake, Oregon. *Contributions to Mineralogy and Petrology* **98**, 224–256.

Baker, D. R. & Eggler, D. H. (1987). Compositions of anhydrous and hydrous melts coexisting with plagioclase, augite, and olivine or low-Ca pyroxene from 1 atm to 8 kbar: application to the Aleutian volcanic center of Atka. *American Mineralogist* **72**, 12–28.

Barclay, J. & Carmichael, I. S. E. (2004). A hornblende basalt from western Mexico: water-saturated phase relations constrain a pressure–temperature window of eruptibility. *Journal of Petrology* **45**, 485–506.

Barton, M., Salters, V. J. M. & Huijsmans, J. P. P. (1983). Sr-isotope and trace element evidence for the role of continental crust in calc-alkaline volcanism on Santorini and Milos, Aegean Sea, Greece. *Earth and Planetary Science Letters* **63**, 273–291.

Berndt, J., Koepke, J. & Holtz, F. (2005). An experimental investigation of the influence of water and oxygen fugacity on differentiation of MORB at 200 MPa. *Journal of Petrology* **46**, 135–167.

Bottinga, Y. & Weill, D. F. (1970). Densities of liquid silicate system calculated from partial molar volumes of oxide components. *American Journal of Science* **269**, 169–182.

Cadoux, A., Scaillet, B., Druitt, T. H. & Deloule, E. (2014). Magma storage conditions of large Plinian eruptions of Santorini. *Journal of Petrology* **55**, 1129–1171.

Chou, I.-M. (1978). Calibration of oxygen buffers at elevated *P* and *T* using the hydrogen fugacity sensor. *American Mineralogist* **63**, 690–703.

Cottrell, E., Gardner, J. E. & Rutherford, M. J. (1999). Petrologic and experimental evidence for the movement and heating of the pre-eruptive Minoan rhyodacite (Santorini, Greece). *Contributions to Mineralogy and Petrology* **135**, 315–331.

Dall'Agnol, R. S., Scaillet, B. & Pichavant, M. (1999). An experimental study of a lower Proterozoic A-type granite from the eastern Amazonia craton, Brazil. *Journal of Petrology* **40**, 1673–1697.

Deer, W. A., Howie, R. A. & Zussman, J. (1972). *Rock-Forming Minerals. Volume 4, Framework Silicates.* Harlow: Longman, 435 pp.

Devine, J. D., Gardner, J. E., Brack, H. P., Layne, G. D. & Rutherford, M. J. (1995). Comparison of microanalytical methods for estimating H_2O contents of silicic volcanic glasses. *American Mineralogist* **80**, 319–328.

Di Carlo, I., Pichavant, M., Rotolo, S. G. & Scaillet, B. (2006). Experimental crystallization of a high-K arc basalt: the golden pumice, Stromboli volcano (Italy). *Journal of Petrology* **47**, 1317–1343.

Druitt, T. H. (2014). New insights into the initiation and venting of the Bronze-Age eruption of Santorini (Greece), from component analysis. *Bulletin of Volcanology* **76**, 794.

Druitt, T. H. & Bacon, C. R. (1989). Petrology of the zoned calc-alkaline magma chamber of Mount Mazama, Crater Lake, Oregon. *Contributions to Mineralogy and Petrology* **101**, 245–259.

Druitt, T. H., Edwards, L., Mellors, R. M., Pyle, D. M., Sparks, R. S. J., Lanphere, M., Davies, M. & Barriero, B. (1999).

Santorini Volcano. *Geological Society of London, Memoirs* **19**, 165 pp.

Druitt, T. H., Costa, F., Deloule, E., Dungan, M. & Scaillet, B. (2012). Decadal to monthly timescales of magma transfer and reservoir growth at a caldera volcano. *Nature* **482**, 7780.

Eichelberger, J. C. (1978). Andesitic volcanism and crustal evolution. *Nature* **275**, 21–27.

Erdmann, S., Martel, C., Pichavant, M. & Kushnir, A. (2014). Amphibole as an archivist of magmatic crystallization conditions: problems, potential, and implications for inferring magma storage prior to the paroxysmal 2010 eruption of Mount Merapi, Indonesia. *Contributions to Mineralogy and Petrology* **167**, 1016.

Fabbro, G. N., Druitt, T. H. & Scaillet, S. (2013). Evolution of the crustal magma plumbing system during the build-up to the 22-ka caldera-forming eruption of Santorini. *Bulletin of Volcanology* **75**, 767.

Freise, M., Holtz, F., Nowak, M., Scoates, J. S. & Strauss, H. (2009). Differentiation and crystallization conditions of basalts from the Kerguelen large igneous province: an experimental study. *Contributions to Mineralogy and Petrology* **158**, 505–527.

Gardner, J. E., Thomas, R. M. E., Jaupart, C. & Tait, S. (1996). Fragmentation of magma during Plinian volcanic eruptions. *Bulletin of Volcanology* **58**, 144–162.

Gertisser, R., Preece, K. & Keller, J. (2009). The Plinian Lower Pumice 2 eruption, Santorini, Greece: Magma evolution and volatile behaviour. *Journal of Volcanology and Geothermal Research* **186**, 387–406.

Giordano, D., Russell, J. K. & Dingwell, D. B. (2008). Viscosity of magmatic liquids: a model. *Earth and Planetary Science Letters* **271**, 123–134.

Hammarstrom, J. M. & Zen, E. A. (1986). Aluminium in hornblende: an empirical igneous geobarometer. *American Mineralogist* **71**, 1297–1313.

Heiken, G. & McCoy, F., Jr (1984). Caldera development during the Minoan eruption, Thira, Cyclades, Greece. *Journal of Geophysical Research* **89**, 8441–8462.

Hildreth, W. & Wilson, C. J. N. (2007). Compositional zoning of the Bishop Tuff. *Journal of Petrology* **48**, 951–999.

Hollister, L. S., Grissom, G. C., Peters, E. K., Stowell, H. H. & Sisson, V. B. (1987). Confirmation of the empirical correlation of Al in hornblende with pressure of solidification of calc-alkaline plutons. *American Mineralogist* **72**, 231–239.

Huijsmans, J. P. P. (1985). *Calc-alkaline lavas from the volcanic complex of Santorini, Aegean Sea, Greece. A petrological, geochemical and stratigraphic study. Geologica Ultraiectina* **41**, 316 pp.

Huijsmans, J. P. P. & Barton, M. (1989). Polybaric geochemical evolution of two shield volcanoes from Santorini, Aegean Sea, Greece: evidence for zoned magma chambers from cyclic compositional variations. *Journal of Petrology* **30**, 583–625.

Huijsmans, J. P. P., Barton, M. & Salters, V. J. M. (1988). Geochemistry and evolution of the calc-alkaline volcanic complex of Santorini, Aegean Sea, Greece. *Journal of Volcanology and Geothermal Research* **34**, 283–306.

Johnson, M. C. & Rutherford, M. J. (1989). Experimental calibration of the aluminum-in-hornblende geobarometer with application to Long Valley caldera (California) volcanic rocks. *Geology* **17**, 837–841.

Jolivet, L. & Faccenna, C. (2000). Mediterranean extension and the Africa–Eurasia collision. *Tectonics* **19**, 1095–1106.

Keller, J., Kraml, M. & Schwarz, M. (2000). Dating major volcanic paroxysms within the deep-sea record: the example of the Thera Formation, Santorini, Greece. In: *Exploring volcanoes: utilization of their resources and mitigation of their hazards: abstracts addresses QE521.5 l38 2000, IAVCEI General Assembly, Bali, Indonesia, July 18–22*, p. 16. ed. Volcanological Survey of Indonesia.

Kress, V. C. & Carmichael, I. S. E. (1991). The compressibility of silicate liquids containing Fe_2O_3 and the effect of composition, temperature, oxygen fugacity and pressure on their redox states. *Contributions to Mineralogy and Petrology* **108**, 82–92.

Laumonier, M., Scaillet, B., Pichavant, M., Champallier, R., Andújar, J. & Arbaret, L. (2014). On the conditions of magma mixing and its bearing on andesite production in the crust. *Nature Communications* **5**, 5607.

Leake, B. E., Woolley, A. R., Arps, C. E. S., et al. (1997). Nomenclature of amphiboles: report of the subcommittee on amphiboles of the International Mineralogical Association Commission on New Minerals and Mineral Names. *Mineralogical Magazine* **61**, 295–321.

Le Bas, M. J. & Streckeisen, A. L. (1991). The IUGS systematics of igneous rocks. *Journal of the Geological Society, London* **148**, 825–833.

Le Pichon, X. & Angelier, J. (1979). The Hellenic arc and trench system: A key to the neotectonic evolution of the eastern Mediterranean area. *Tectonophysics* **60**, 1–42.

Libourel, G. (1999). Systematics of calcium partitioning between olivine and silicate melt: implications for melt structure and calcium content of magmatic olivines. *Contributions to Mineralogy and Petrology* **136**, 63–80.

Mandeville, C. W., Carey, S. & Sigurdsson, H. (1996). Magma mixing, fractional crystallization and volatile degassing during the 1883 eruption of Krakatau volcano, Indonesia. *Journal of Volcanology and Geothermal Research* **74**, 243–274.

Mann, A. C. (1983). Trace element geochemistry of high alumina basalt–andesite–dacite–rhyodacite lavas of the Main Volcanic Series of Santorini Volcano, Greece. *Contributions to Mineralogy and Petrology* **395**, 43–57.

Martel, C., Pichavant, M., Holtz, F. & Scaillet, B. (1999). Effects of fO_2 and H_2O on andesite phase relations between 2 and 4 kbar. *Journal of Geophysical Research* **104**, 29453–29470.

Martin, V., Holness, M. & Pyle, D. (2006). Textural analysis of magmatic enclaves from the Kameni Islands, Santorini, Greece. *Journal of Volcanology and Geothermal Research* **154**, 89–102.

Michaud, V., Clocchiatti, R. & Sbrana, S. (2000). The Minoan and post-Minoan eruptions, Santorini (Greece), in the light of melt inclusions: chlorine and sulphur behaviour. *Journal of Volcanology and Geothermal Research* **99**, 195–214.

Miyashiro, A. (1974). Volcanic rock series in island arcs and active continental margins. *American Journal of Science* **274**, 321–355.

Morgan, G. B. & London, D. (2005). Effect of current density on the electron microprobe analysis of alkali aluminosilicate glasses. *American Mineralogist* **90**, 1131–1138.

Morimoto, N. (1989). Nomenclature of pyroxenes. Subcommittee on pyroxenes. Commission on new minerals and mineral names. *Canadian Mineralogist* **27**, 143–156.

Mortazavi, M. & Sparks, R. S. J. (2004). Origin of rhyolite and rhyodacite lavas and associated mafic inclusions of Cape Akrotiri, Santorini: the role of wet basalt in generating calc-alkaline silicic magmas. *Contributions to Mineralogy and Petrology* **146**, 397–413.

Nicholls, I. A. (1971a). Petrology of Santorini volcano, Cyclades, Greece. *Journal of Petrology* **12**, 67–119.

Nicholls, I. A. (1971b). Calcareous inclusions in lavas and agglomerates of Santorini volcano. *Contributions to Mineralogy and Petrology* **30**, 261–276.

Papale, P., Moretti, R. & Barbato, D. (2006). The compositional dependence of the saturation surface of $H_2O + CO_2$ fluids in silicate melts. *Chemical Geology* **229**, 78–95.

Papazachos, B. C., Karakostas, V. G., Papazachos, C. B. & Scordilis, E. M. (2000). The geometry of the Wadati–Benioff zone and lithospheric kinematics in the Hellenic arc. *Tectonophysics* **319**, 275–300.

Parat, F., Streck, M. J., Holtz, F. & Almeev, R. (2014). Experimental study into the petrogenesis of crystal-rich basaltic to andesitic magmas at Arenal volcano. *Contributions to Mineralogy and Petrology* **168**, 1040.

Parks, M. M., Biggs, J., England, P., Mather, T. A., Nomikou, P., Palamartchouk, K., Papanikolaou, X., Paradissis, D., Parsons, B., Pyle, D. M., Raptakis, C. & Zacharis, V. (2012). Evolution of Santorini Volcano dominated by episodic and rapid fluxes of melt from depth. *Nature Geoscience* **5**, 749–754.

Pichavant, M. & Macdonald, R. (2007). Crystallization of primitive basaltic magmas at crustal pressures and genesis of the calc-alkaline igneous suite: experimental evidence from St. Vincent, Lesser Antilles arc. *Contributions to Mineralogy and Petrology* **154**, 535–558.

Pichavant, M., Martel, C., Bourdier, J.-L. & Scaillet, B. (2002). Physical conditions, structure and dynamics of a zoned magma chamber: Mt. Pelée (Martinique, Lesser Antilles arc). *Journal of Geophysical Research* **107**, doi:10.1029/2001JB000315.

Pichavant, M., Costa, F., Burgisser, A., Scaillet, B., Martel, C. & Poussineau, S. (2007). Equilibration scales in silicic to intermediate magmas—implications for phase equilibrium studies. *Journal of Petrology* **48**, 1955–1972.

Pichavant, M., Di Carlo, I., Le Gac, Y., Rotolo, S. G. & Scaillet, B. (2009). Experimental constraints on the deep magma feeding system at Stromboli volcano, Italy. *Journal of Petrology* **50**, 601–624.

Pichavant, M., Scaillet, B., Pommier, A., Iacono-Marziano, G. & Cioni, R. (2014). Nature and evolution of primitive Vesuvius magmas: an experimental study. *Journal of Petrology* **55**, 2281–2310.

Pownceby, M. I. & O'Neill, H. St. C. (1994). Thermodynamic data redox reactions at high temperatures. III. Activity–composition relations in Ni–Pd alloys from EMF measurements at 850–1250 K, and calibration of the $NiO + Ni$–Pd assemblage as a redox sensor. *Contributions to Mineralogy and Petrology* **116**, 327–339.

Pyle, D. & Elliott, J. (2006). Quantitative morphology, recent evolution, and future activity of the Kameni Islands volcano, Santorini, Greece. *Geosphere* **2**, 253–268.

Reilinger, R., McClusky, S., Paradissis, D., Ergintav, S. & Vernant, P. (2010). Geodetic constraints on the tectonic evolution of the Aegean region and strain accumulation along the Hellenic subduction zone. *Tectonophysics* **488**, 22–30.

Reubi, O. & Blundy, J. (2009). A dearth of intermediate melts at subduction zone volcanoes and the petrogenesis of arc andesites. *Nature* **461**, 1269–1273.

Ridolfi, F. & Renzulli, A. (2012). Calcic amphiboles in calc-alkaline and alkaline magmas: thermobarometric and chemometric empirical equations valid up to 1130°C and 2·2 GPa. *Contributions to Mineralogy and Petrology* **163**, 877–895.

Robie, R. A., Hemingway, B. S. & Fisher, J. R. (1979). *Thermodynamic properties of minerals and related substances at 298·15 K and 1 bar (105 pascals) pressure and at higher temperatures. US Geological Survey Bulletin* **1452**, 456 pp.

Scaillet, B. & Evans, B. W. (1999). The 15 June 1991 eruption of Mount Pinatubo. I. phase equilibria and Pre-eruption P-T-fO$_2$-aH$_2$O. *Journal of Petrology* **40**, 381–411.

Scaillet, B. & Macdonald, R. (2006). Experimental and thermodynamic constraints on the sulphur yield of peralkaline and metaluminous silicic flood eruptions. *Journal of Petrology* **47**, 1413–1437.

Scaillet, B., Pichavant, M. & Roux, J. (1995). Experimental crystallization of leucogranites magmas. *Journal of Petrology* **36**, 663–705.

Schmidt, M. W. (1992). Amphibole composition in tonalite as a function of pressure; an experimental calibration of the Al-in-hornblende barometer. *Contributions to Mineralogy and Petrology* **110**, 304–310.

Self, S., Gertisser, R., Thordarson, T., Rampino, M. R. & Wolff, J. A. (2004). Magma volume, volatile emissions, and stratospheric aerosols from the 1815 eruption of Tambora. *Geophysical Research Letters* **31**, L20608.

Sisson, T. W. & Grove, T. L. (1993a). Experimental investigations of the role of H$_2$O in calc-alkaline differentiation and subduction zone magmatism. *Contributions to Mineralogy and Petrology* **113**, 143–166.

Sisson, T. W. & Grove, T. L. (1993b). Temperatures and H$_2$O contents of low-MgO high-alumina basalts. *Contributions to Mineralogy and Petrology* **113**, 167–184.

Taylor, J. R., Wall, V. J. & Pownceby, M. I. (1992). The calibration and application of accurate redox sensors. *American Mineralogist* **77**, 284–295.

Toplis, M. J. & Carroll, M. R. (1995). An experimental study of the influence of oxygen fugacity on Fe–Ti oxide stability, phase relations, and mineral–melt equilibria in ferro-basaltic systems. *Journal of Petrology* **36**, 1137–1170.

Vespa, M., Keller, J. & Gertisser, R. (2006). Interplinian explosive activity of Santorini volcano (Greece) during the past 150,000 years. *Journal of Volcanology and Geothermal Research* **153**, 262–286.

Zellmer, G., Turner, S. & Hawkesworth, C. (2000). Timescales of destructive plate margin magmatism: new insights from Santorini, Aegean volcanic arc. *Earth and Planetary Science Letters* **174**, 265–281.